

Quench dynamics of the quantum XXZ chain with staggered interactions: Exact results and simulations on digital quantum computers

Ching-Tai Huang,¹ Yu-Cheng Lin ^{1,*} and Ferenc Iglói ^{2,3,†}

¹Graduate Institute of Applied Physics, National Chengchi University, Taipei 11605, Taiwan

²Wigner Research Centre for Physics, Institute for Solid State Physics and Optics, H-1525 Budapest, Hungary

³Institute of Theoretical Physics, University of Szeged, H-6720 Szeged, Hungary

We investigate quench dynamics in the quantum $S = 1/2$ XXZ antiferromagnetic chain with staggered and anisotropic interactions in the flat-band limit. Our quench protocol interchanges the odd- and even-bond strengths of a fully dimerized chain, enabling us to derive exact time-dependent states for arbitrary even system sizes by working in the Bell basis. We obtain closed-form, size-independent expressions for the von Neumann and second-order Rényi entanglement entropies. We further calculate exact Loschmidt echoes and the corresponding return rate functions across various anisotropies and system sizes, and identify Loschmidt zeros in finite chains. Our analysis reveals distinct finite-size scaling of the Loschmidt echo at critical times with chain length and identifies the precise conditions on the anisotropy parameter governing the periodicity of the dynamical observables. In addition to the analytic study, we perform two types of numerical experiments on IBM-Q quantum devices. First, we use the Hadamard test to estimate the Bell-basis expansion coefficients and reconstruct the dynamical states, achieving accurate entanglement entropies and the Loschmidt echo for small systems. Second, we implement Trotter-error-free time-evolution circuits combined with randomized Pauli measurements. Post-processing via statistical correlations and classical shadows yields reliable estimates of the second-order Rényi entanglement entropy and the Loschmidt echo, showing satisfactory agreement with exact results.

I. INTRODUCTION

Over the past decades, non-equilibrium dynamics of closed quantum systems has become an intensively studied topic, both theoretically and experimentally. Among experimental platforms, ultracold atomic systems offer an ideal setting for exploring such quantum dynamics [1–5]. More recently, rapid advances in programmable quantum devices based on various types of physical qubits have opened new avenues for probing the dynamics of quantum many-body systems [6–16].

Central questions in this field concern the nature of relaxation and the long-time behavior following a quantum quench, i.e. a sudden change in the Hamiltonian parameters [17]. In homogeneous systems with extended eigenstates, local observables typically relax exponentially fast, and the stationary state depends on whether the underlying Hamiltonian is integrable or non-integrable. Non-integrable systems are expected to thermalize, reaching a stationary state described by a Gibbs ensemble with an effective temperature [18–21]. On the other hand, integrable systems, characterized by an extensive number of conserved quantities, typically equilibrate to non-thermal stationary states described by a so-called generalized Gibbs ensemble [22–29].

There also exist systems that fail to relax after a quench. Several mechanisms can lead to a lack of relaxation, including confinement [30–32], flat band [33, 34], disorder [35, 36], and many-body quantum scars [37, 38]. Absence of relaxation is often reflected in the growth and spreading of entanglement; one scenario is persistent and long-lived entanglement oscillations even in the infinite-size limit.

In this paper, we investigate quench dynamics of the quantum $S = 1/2$ XXZ antiferromagnetic chain with staggered and anisotropic interactions in the flat-band limit. We consider global quenches implemented by interchanging the odd- and even-bond strengths in a fully dimerized XXZ chain. This system fails to relax at long times after the quench due to the vanishing group velocity of its excitations. We derive a formula for the time-dependent states in the Bell basis for arbitrary finite system size, and obtain closed-form solutions for dynamical entanglement entropies quantified by both the von Neumann and the second-order Rényi entropies. We also compute the exact Loschmidt echo, identify Loschmidt zeros in certain finite chains, and determine analytical expressions for a variety of anisotropy parameters and system sizes. From these exact results, we establish the conditions on the combined parameter $J\Delta$, the product of bond strength J and anisotropy Δ , that determine the periodicity or non-periodicity of the dynamical observables. Furthermore, we uncover special finite-size scaling behaviors of the Loschmidt echo at dynamical phase transitions, which, to the best of our knowledge, have not been reported previously.

In addition, we perform numerical experiments on the IBM-Q quantum processors. In one experiment, we estimate the coefficients of the initial state in the Bell basis using the Hadamard test [39] and reconstruct the time-dependent state from these coefficients to obtain dynamical entanglement entropies and the Loschmidt echo for various values Δ . In a second experiment, we implement quantum circuits for the time evolution and measure the evolved states in randomly selected Pauli bases. Using classical post-processing of these measurement outcomes via statistical correlations and classical shadows [40–44], we estimate the second-order Rényi entanglement entropy and the Loschmidt echo.

The paper is organized as follows: In Sec. II, we define the model and the quench protocols considered in this study; we

* yc.lin@nccu.edu.tw

† igloi.ferenc@wigner.hun-ren.hu

review the Bell basis and describe how to reconstruct the time-dependent states by working in this basis. In this section, the definitions and properties of the entanglement entropies and the Loschmidt echo are also given. In Sec. III, we present the derivations of the dynamical entanglement entropies and the Loschmidt echo for our model, and provide exact solutions for these observables for certain finite chains. In Sec. IV, we describe our simulation setups on the IBM-Q devices and present our simulation results, using the Hadamard test and randomized measurements. We conclude in Sec. V with a summary and discussion. In the Appendices, some analytical expressions are explicitly given.

II. MODEL AND ITS NON-EQUILIBRIUM DYNAMICS

We consider global quantum quenches in the dimerized spin-1/2 XXZ Heisenberg chain with alternating bond strengths, defined by the Hamiltonian of $N = 2n$ spins

$$\mathcal{H}(J, J', \Delta) = \mathcal{H}_1(J, \Delta) + \mathcal{H}_2(J', \Delta), \quad (1)$$

with

$$\mathcal{H}_1(J, \Delta) = \sum_{i=1}^n J (S_{2i-1}^x S_{2i}^x + S_{2i-1}^y S_{2i}^y + \Delta S_{2i-1}^z S_{2i}^z) \quad (2)$$

and

$$\mathcal{H}_2(J', \Delta) = \sum_{i=1}^n J' (S_{2i}^x S_{2i+1}^x + S_{2i}^y S_{2i+1}^y + \Delta S_{2i}^z S_{2i+1}^z) \quad (3)$$

where S_i^α , $\alpha = x, y, z$ are the spin-1/2 operators at site i , J and J' are positive coupling constants on odd and even links, respectively. The parameter Δ characterizes the anisotropy in the interaction. For periodic boundary conditions (PBC), we have $S_{2n+1}^\alpha = S_1^\alpha$. In some cases, we consider chains with open boundary conditions (OBC), i.e.

$$\mathcal{H}_2(J', \Delta) = \sum_{i=1}^{n-1} J' (S_{2i}^x S_{2i+1}^x + S_{2i}^y S_{2i+1}^y + \Delta S_{2i}^z S_{2i+1}^z). \quad (4)$$

For $\Delta = 0$, the model reduces to the XX chain, which can be mapped to well-studied free-fermion systems [45, 46]. At $\Delta = 1$, the system becomes the XXX chain: in the uniform case ($J = J'$), it is exactly solvable via the Bethe ansatz [47], while in the dimerized case it exhibits the well-known spin-Peierls transition [48, 49].

We initialize the system at $t = 0$ in the ground state $|\Psi_0\rangle$ of the fully dimerized Hamiltonian $\mathcal{H}(J, 0, \Delta) = \mathcal{H}_1(J, \Delta)$ with $J > 0$, corresponding to a product of singlet dimers on odd links. The state then evolves unitarily under $\mathcal{H}(0, J, \Delta) = \mathcal{H}_2(J, \Delta)$, corresponding to a sudden interchange of the odd and even bond strengths. In this setting, both the prequench and postquench Hamiltonians can be written as sums of non-interacting dimers:

$$\mathcal{H}_1(J, \Delta) = \sum_i^n h_{2i-1}, \quad \mathcal{H}_2(J, \Delta) = \sum_i^n h_{2i}, \quad (5)$$

with

$$h_j = J(S_j^x S_{j+1}^x + S_j^y S_{j+1}^y + \Delta S_j^z S_{j+1}^z). \quad (6)$$

Each dimer has eigenstates given by the Bell states, which can be expressed in the S^z -basis (Z -basis), $|0\rangle$ and $|1\rangle$, as

$$\begin{aligned} |\psi_0(j)\rangle &= \frac{1}{\sqrt{2}}(|0_j 1_{j+1}\rangle - |1_j 0_{j+1}\rangle), & \epsilon_0 &= -\frac{J}{4}(2 + \Delta) \\ |\psi_1(j)\rangle &= \frac{1}{\sqrt{2}}(|0_j 1_{j+1}\rangle + |1_j 0_{j+1}\rangle), & \epsilon_1 &= \frac{J}{4}(2 - \Delta) \\ |\psi_2(j)\rangle &= \frac{1}{\sqrt{2}}(|0_j 0_{j+1}\rangle + |1_j 1_{j+1}\rangle), & \epsilon_2 &= \frac{J}{4}\Delta \\ |\psi_3(j)\rangle &= \frac{1}{\sqrt{2}}(|0_j 0_{j+1}\rangle - |1_j 1_{j+1}\rangle), & \epsilon_3 &= \frac{J}{4}\Delta \end{aligned} \quad (7)$$

where the corresponding energy eigenvalues are denoted by ϵ_μ , $\mu = 0, 1, 2, 3$. We use $|0\rangle$ to denote the spin-up state, and $|1\rangle$ the spin-down state.

The initial state can then be written as a product state:

$$|\Psi_0\rangle = \prod_{i=1}^n |\psi_0(2i-1)\rangle \quad (8)$$

Similarly, the k -th eigenstate Φ_k ($k = 1, 2, \dots, 2^{2n}$) of the postquench Hamiltonian $\mathcal{H}(0, J, \Delta)$ is given by:

$$|\Phi_k\rangle = \prod_{i=1}^n |\psi_{i_k}(2i)\rangle, \quad i_k = 0, 1, 2, 3 \quad (9)$$

with corresponding energies

$$E_k = \sum_{i=1}^n \epsilon_{i_k}, \quad i_k = 0, 1, 2, 3. \quad (10)$$

Expanding $|\Psi_0\rangle$ in terms of $|\Phi_k\rangle$:

$$|\Psi_0\rangle = \sum_k a_k |\Phi_k\rangle, \quad (11)$$

we obtain the time-evolved state

$$\begin{aligned} |\Psi_0(t)\rangle &= \sum_{k=1}^{\mathcal{N}} a_k(t) |\Phi_k\rangle \\ &= \sum_{k=1}^{\mathcal{N}} a_k \exp(-iE_k t) |\Phi_k\rangle, \end{aligned} \quad (12)$$

where $\mathcal{N} = 2^{2n}$. The expansion coefficients $a_k = \langle \Phi_k | \Psi_0 \rangle$, given by scalar products between products of Bell states and singlet states, are all real. Once the set of Δ -independent coefficients a_k is known, the time-dependent state at any t under the postquench Hamiltonian with arbitrary anisotropy parameter Δ can be determined.

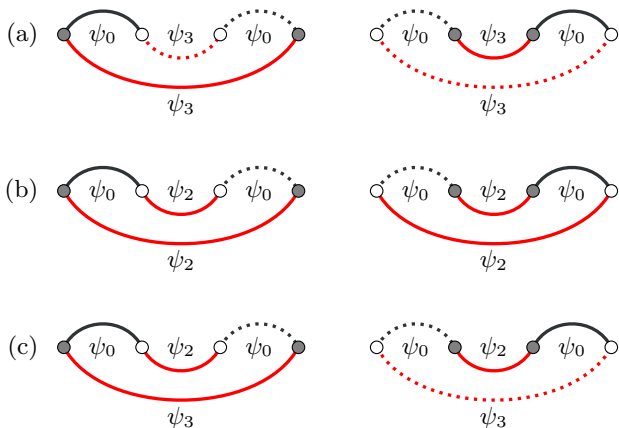


FIG. 1. Overlap diagrams for a positive (a), negative (b) and zero (c) coefficient $a_k = \langle \Phi_k | \Psi_0 \rangle$ in a four-site chain with PBC. Gray and white circles represent spin-up state $|0\rangle$ and spin-down state $|1\rangle$, respectively. Black and red arches represent valence bonds (Bell dimers) ψ_i in the states $|\Psi_0\rangle$ and $|\Phi_k\rangle$, with solid (dotted) arches indicating positive (negative) contributions determined by the spin orientations. In each panel, the right diagram is obtained from the left by a global spin inversion. In (a), two negative dimers remain under spin inversion, resulting in a positive coefficient $a_k = 2 \cdot 2^{-2}$; in (b), one negative dimer remains, corresponding to a negative coefficient $a_k = -2 \cdot 2^{-2}$; in (c) the number of negative dimers change from one to two after spin inversion, representing a case with zero coefficient $a_k = 0$.

A. Expansion coefficients a_k

The scalar product for a coefficient a_k can be written in terms of spin states in Z -basis $|Z\rangle = |z_1 z_2 \cdots z_N\rangle$ as

$$a_k = \langle \Phi_k | \Psi_0 \rangle = \frac{1}{2^n} \sum_{Z'Z} \langle Z' | Z \rangle \sigma' \sigma, \quad (13)$$

where σ and σ' are the signs of the states $|Z\rangle$ and $|Z'\rangle$, respectively. In this expression, only the terms with $Z = Z'$ contribute.

Alternatively, a_k can be formulated as the overlap between the two states $|\Phi_k\rangle$ and $|\Psi_0\rangle$ in the valence-bond basis. A valence bond here refers to a singlet or triplet dimer, i.e. a Bell state. In this paper, this basis is also referred to as the Bell basis. For a given dimer configuration in $|\Phi_k\rangle$ ($|\Psi_0\rangle$ is a fixed set of singlet dimers) in a chain with PBC, the overlap is determined by a single closed loop in the transition graph in which the singlet-triplet dimers of two states are superimposed [50, 51] [cf. Fig. 1]. The spin configurations on the loop must be consistent with the dimer configurations in both $|\Phi_k\rangle$ and $|\Psi_0\rangle$. There exist two compatible spin configurations related by global spin inversion, resulting in possible finite overlaps: $a_k = \pm 2 \cdot 2^{-n}$, where the factor 2^{-n} arises from the normalization in Eq. (13).

The sign of the overlap depends on the dimer types and the spin orientations along the loop. For instance, a dimer in the triplet state $|\psi_3\rangle = (|00\rangle - |11\rangle)/\sqrt{2}$ contributes positively when connecting two up-spins, but negatively when

connecting two down-spins. Consequently, a loop containing an even (odd) number of such negative dimers produces a positive (negative) overlap. In certain cases, the overlap vanishes because the loop changes sign under a global spin flip. Figure 1 illustrates some cases for positive, negative and zero overlaps (coefficients).

Since all nonzero coefficients are of equal magnitude $|a_k| = 2^{-(n-1)}$, normalization of $|\Psi_0(t)\rangle$ requires exactly $\mathcal{N}^* = 4^{n-1}$ nonzero coefficients. Thus, the coefficients a_k are given by

$$a_k = \begin{cases} \pm 2^{-(n-1)}, & \text{for } k \in k^* = 1, 2, \dots, 4^{n-1} \\ 0, & \text{otherwise,} \end{cases} \quad (14)$$

where k^* denotes the set of indices for nonzero a_k .

By encoding the Bell states as $(\psi_0, \psi_1, \psi_2, \psi_3) = (0, 1, 2, 3)$, we have identified two selection rules for all dimer configurations in $|\Phi_k\rangle$ [Eq. (11)] with nonzero a_k :

- (1) the sum of all dimer-type indices $\sum_{i=1}^n \psi_{i_k}$ must be even; and
- (2) the combined count of ψ_2 and ψ_3 dimers must also be even.

B. Dynamical quantities

We are interested in the time evolution of the entanglement entropy and the Loschmidt echo. The former characterizes how entanglement spreads through the system after a quantum quench; the latter serves as the observable for identifying dynamical phase transitions.

The entanglement entropy (EE) quantifies the degree of quantum entanglement between a subsystem and its complement. For a time-evolved state $|\Psi_0(t)\rangle$ partitioned into two parts A and B , the entanglement between them is encoded in the reduced density matrix of one part, say A ,

$$\rho_A(t) = \text{Tr}_B |\Psi_0(t)\rangle \langle \Psi_0(t)|, \quad (15)$$

where Tr_B denotes the partial trace over B . We consider both the von Neumann EE, defined by

$$\mathcal{S}_1(t) = -\text{Tr} [\rho_A(t) \log_2 \rho_A(t)], \quad (16)$$

and the second-order Rényi EE, given by

$$\mathcal{S}_2(t) = -\log_2 \text{Tr} [\rho_A^2(t)]. \quad (17)$$

For the quench protocols studied here, both the von Neumann and Rényi EE exhibit persistent oscillations, indicating the absence of relaxation due to confinement [30, 31]. Such persistent entanglement oscillations have been previously reported in the fully dimerized XX chain with $\Delta = 0$ (equivalently, the flat-band Su-Schrieffer-Heeger chain) [13, 52]. Here we extend this analysis to the XXZ chain with $\Delta \neq 0$.

The Loschmidt echo, also known as the return probability, quantifies the overlap between the initial state $|\Psi_0\rangle$ and its time-evolved counterpart $|\Psi_0(t)\rangle$ [53–59]:

$$\mathcal{L}(t) = |\langle \Psi_0 | \Psi_0(t) \rangle|^2 = |\langle \Psi_0 | \exp(-i\mathcal{H}_2(J, \Delta)t) | \Psi_0 \rangle|^2. \quad (18)$$

In the limit of large N , the Loschmidt echo has an asymptotic form given by

$$\mathcal{L}(t) = \exp(-Nr(t)), \quad (19)$$

where $r(t)$ expressed as

$$r(t) = -\frac{1}{N} \ln \mathcal{L}(t), \quad (20)$$

is known as the return rate function.

The Loschmidt echo can be interpreted as the squared magnitude of an out-of-equilibrium analog of the partition function in equilibrium statistical mechanics. In the thermodynamic limit, zeros in the Loschmidt echo signal a dynamical phase transition, with singularities appearing in the return rate function [53–59]. Exact zeros of the Loschmidt echo can also occur in finite-size systems under certain conditions, as reported in recent studies [60–62]. In this work, we identify finite-size Loschmidt zeros in our quench experiments for specific anisotropy parameters.

III. EXACT RESULTS

Here we show the results for finite chains, obtained by evaluating the expressions in Eqs. (16), (17) and (18).

A. Half-chain entanglement entropy

We consider the entanglement between two halves of the chain with PBC, quantified by the von Neumann entropy and the second-order Rényi entropy. Without loss of generality, we set one boundary between site $i = n$ and $i = n + 1$ and the other between site $i = 2n$ and $i = 1$.

The key ingredient of the entanglement entropy is the reduced density matrix, ρ_A , of the subsystem considered. Here for a half chain, the dimension of the reduced density matrix is $2^n \times 2^n$. Using the eigenvalues of ρ_A , that are all real and satisfy $0 \leq \lambda_l(t) \leq 1$, $\sum_{l=1}^{2^n} \lambda_l(t) = 1$, we obtain the von Neumann EE by

$$\mathcal{S}_1(t) = -\sum_{l=1}^{2^n} \lambda_l(t) \log_2[\lambda_l(t)], \quad (21)$$

and the Rényi EE by

$$\mathcal{S}_2(t) = -\log_2 \sum_{l=1}^{2^n} \lambda_l^2(t). \quad (22)$$

1. $n = 2$

We start with the shortest chain with $n = 2$. There are four nonzero coefficients $a_1 = a_2 = a_4 = 1/2$ and $a_3 = -1/2$

contributed by the following dimer configurations in $|\Phi_k\rangle$:

$$\begin{aligned} |\Phi_1\rangle &= |\psi_0(2)\rangle |\psi_0(4)\rangle, \\ |\Phi_2\rangle &= |\psi_1(2)\rangle |\psi_1(4)\rangle, \\ |\Phi_3\rangle &= |\psi_2(2)\rangle |\psi_2(4)\rangle, \\ |\Phi_4\rangle &= |\psi_3(2)\rangle |\psi_3(4)\rangle, \end{aligned} \quad (23)$$

with energies $E_1 = -J(2 + \Delta)/2$, $E_2 = J(2 - \Delta)$ and $E_3 = E_4 = J\Delta/2$. The time-evolved state $|\Psi_0(t)\rangle$ in the spin basis is then given by

$$\begin{aligned} |\Psi_0(t)\rangle &= \frac{1}{4}(1/e^+ + e^-)(|1010\rangle + |0101\rangle) \\ &\quad - \frac{1}{2}e^0(|1001\rangle + |0110\rangle) \\ &\quad + \frac{1}{4}(-1/e^+ + e^-)(|1100\rangle + |0011\rangle), \end{aligned} \quad (24)$$

where the shorthand notations $e^\pm = \exp[-i(1 \pm \Delta/2)Jt]$ and $e^0 = \exp[-i(\Delta/2)Jt]$ are used. The reduced density matrix for the first half of the chain in terms of the basis $|00\rangle, |01\rangle, |10\rangle$ and $|11\rangle$ is given by:

$$\begin{bmatrix} \frac{1}{4} \sin^2 Jt & 0 & 0 & 0 \\ 0 & \frac{1}{4}(1 + \cos^2 Jt) & -\frac{1}{2} \cos Jt \cos \Delta Jt & 0 \\ 0 & -\frac{1}{2} \cos Jt \cos \Delta Jt & \frac{1}{4}(1 + \cos^2 Jt) & 0 \\ 0 & 0 & 0 & \frac{1}{4} \sin^2 Jt \end{bmatrix}, \quad (25)$$

which has the eigenvalues:

$$\begin{aligned} \lambda_{1,2} &= \frac{1}{4} \sin^2(Jt) \\ \lambda_{3,4} &= \frac{1}{4} [1 + \cos^2(Jt) \pm 2 \cos(Jt) \cos(J\Delta t)]. \end{aligned} \quad (26)$$

Thus, the von Neumann EE can be obtained by inserting the eigenvalues into Eq. (21), yielding

$$\begin{aligned} \mathcal{S}_1^{n=2}(t) &= 2 - \frac{1}{2} \sin^2(Jt) \log_2 \sin^2(Jt) \\ &\quad - \frac{1}{4} [1 + \cos^2(Jt) + 2 \cos(Jt) \cos(J\Delta t)] \\ &\quad \times \log_2 [1 + \cos^2(Jt) + 2 \cos(Jt) \cos(J\Delta t)] \\ &\quad - \frac{1}{4} [1 + \cos^2(Jt) - 2 \cos(Jt) \cos(J\Delta t)] \\ &\quad \times \log_2 [1 + \cos^2(Jt) - 2 \cos(Jt) \cos(J\Delta t)]. \end{aligned} \quad (27)$$

Similarly, the Rényi EE is obtained from Eq. (22):

$$\begin{aligned} \mathcal{S}_2^{n=2}(t) &= 3 - \log_2 [1 + \sin^4(Jt) + 2 \cos^2(Jt) \\ &\quad + \cos^4(Jt) + 4 \cos^2(Jt) \cos^2(J\Delta t)]. \end{aligned} \quad (28)$$

Both functions $\mathcal{S}_1^{n=2}(t)$ and $\mathcal{S}_2^{n=2}(t)$ reach their maximum value of 2, independent of Δ , at $t = (2m + 1)\pi/2J$ with $m = 0, 1, 2, \dots$ when the condition $\cos(Jt) = 0$ is satisfied.

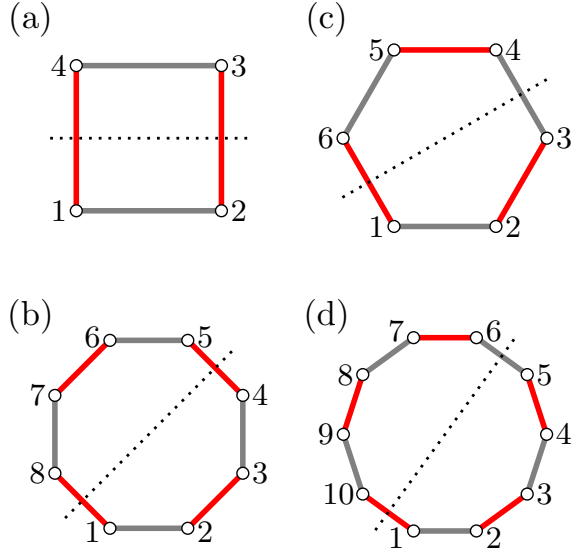


FIG. 2. Sketch of the bipartition for chains with PBC and $n = 2, 3, 4, 5$. Gray lines denote the singlet dimers in the initial state $|\Psi_0\rangle$, and red lines represent the couplings of the postquench Hamiltonian. The dotted line in each figure marks a symmetric bipartition of the chain. (a) and (b): For even n , the bipartition cuts two couplings of the post-quench Hamiltonian. (c) and (d): For odd n , the bipartition cuts one postquench coupling and one dimer in the initial state.

For the XX-chain with $\Delta = 0$, the expression for the von Neumann EE is reduced to

$$\mathcal{S}_{1,\text{XX}}^{n=2}(t) = -2 \left[\sin^2\left(\frac{Jt}{2}\right) \log_2 \sin^2\left(\frac{Jt}{2}\right) + \cos^2\left(\frac{Jt}{2}\right) \log_2 \cos^2\left(\frac{Jt}{2}\right) \right], \quad (29)$$

and for the Rényi EE is

$$\mathcal{S}_{2,\text{XX}}^{n=2}(t) = -2 \log_2 [1 - \sin^2(Jt)/2], \quad (30)$$

as also known from free-fermion calculations [13, 63].

$$2. \quad n = 3, 5, \dots$$

For $n = 3$, the eigenvalues of the 8×8 reduced density matrix are

$$\begin{aligned} \lambda_{1,2,3,4} &= \frac{1}{8} \sin^2\left(\frac{Jt}{2}\right) \\ \lambda_{5,6} &= \frac{1}{8} \left[1 + \cos^2\left(\frac{Jt}{2}\right) + 2 \cos\left(\frac{Jt}{2}\right) \cos\left(\frac{J\Delta t}{2}\right) \right] \\ \lambda_{7,8} &= \frac{1}{8} \left[1 + \cos^2\left(\frac{Jt}{2}\right) - 2 \cos\left(\frac{Jt}{2}\right) \cos\left(\frac{J\Delta t}{2}\right) \right]. \end{aligned} \quad (31)$$

These eigenvalues at t are related to those of the $n = 2$ case [see Eq. (26)] by

$$\lambda^{n=3}(t) = \frac{1}{2} \lambda^{n=2}(t/2). \quad (32)$$

Consequently, the entanglement entropies \mathcal{S}_1 and \mathcal{S}_2 for $n = 2$ and $n = 3$ satisfy $\mathcal{S}^{n=3}(t) = 1 + \mathcal{S}^{n=2}(t/2)$. More generally, this relation holds for any odd n ,

$$\mathcal{S}^{n=\text{odd}}(t) = 1 + \mathcal{S}^{n=2}(t/2), \quad (33)$$

and arises from the behavior of the local states at the boundaries of the bipartition.

To clarify this, Fig. 2 illustrates the initial singlet-product state (gray lines) and the couplings (red lines) in the postquench Hamiltonian for chains of length $n = 2, 4$ (Fig. 2(a) and (b)) and $n = 3, 5$ (Fig. 2 (c) and (d)), where the dashed line indicates the symmetric bipartition. In our setup, each initial entangled dimer located at $(i, i + 1)$ can spread over three lattice spacings, covering sites from $i - 1$ to $i + 2$, during the time evolution [13, 63]. The EE of a half chain is the number of entangled states that connect sites inside the partition to sites outside. For any odd $n > 2$, the initial state always contains an entangled dimer that crosses the boundary between sites $i = n$ and $i = n + 1$, contributing a time-independent unit to the EE; this is the constant term '1' in Eq. (33). In addition, at most two entangled states may cross the boundary between sites $i = 1$ and $i = 2n$, evolved from the singlets initially at $(1, 2)$ and $(2n - 1, 2n)$. This time-dependent part of the EE is analogous to the $n = 2$ case. However, in the $n = 2$ chain, the short chain length forces a single entangled state to cross both boundaries simultaneously, whereas for $n > 2$ it can cross only one boundary. As a result, one unit of the EE in the $n = 2$ case involves two couplings with a total strength $2J$ in the postquench Hamiltonian (red lines in Fig. 2), while for $n > 2$ it involves only a single postquench coupling of strength J . This difference leads to a doubling of the entanglement oscillation period for odd $n > 2$ compared with the $n = 2$ case.

$$3. \quad n = 4, 6, \dots$$

Repeating the above reasoning, we can also find an exact relation between the dynamical EE of even $n > 2$ and that of $n = 2$. Similar to the $n = 2$ case, no singlet-dimer initially crosses the bipartition boundaries. The dynamical EE arises solely from two pairs of dimers initially located adjacent to the boundaries, one pair at $(n, n - 1)$ and $(n + 1, n + 2)$, and the other at $(1, 2)$ and $(2n - 1, 2n)$. For $n > 2$, each pair of dimers is connected through one postquench coupling of strength J , and each dimer can cross only one boundary during the time evolution. In contrast, in a $n = 2$ chain there exists only one such pair coupled through two postquench couplings ($2J$), and each entangled state crosses the two boundaries at the same time. Therefore, the dynamical EE for even $n > 2$ is related to that of the $n = 2$ case by

$$\mathcal{S}^{n=\text{even}}(t) = 2\mathcal{S}^{n=2}(t/2), \quad (34)$$

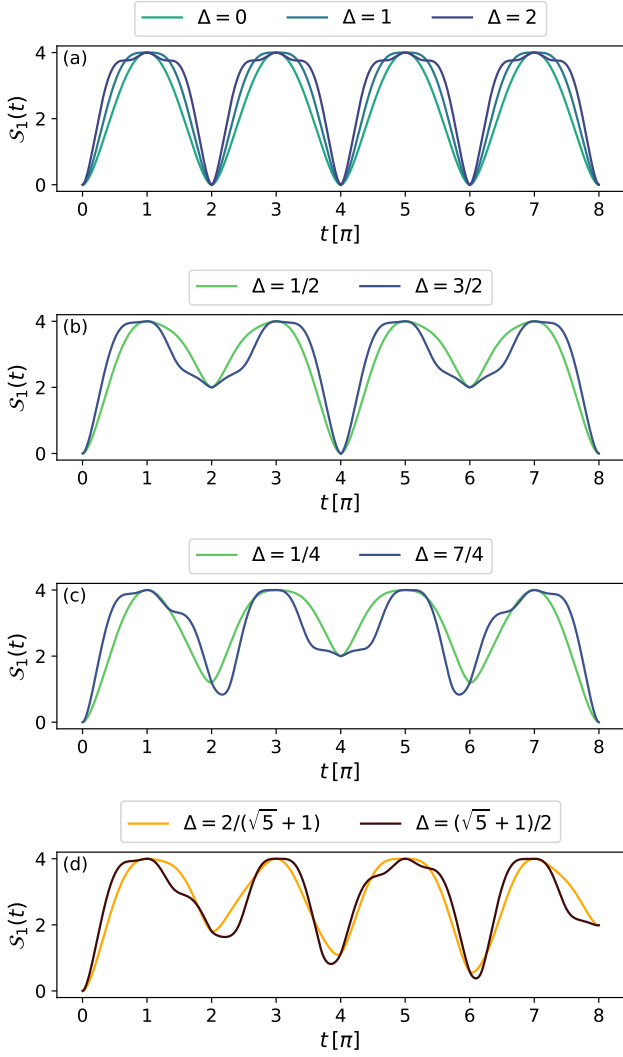


FIG. 3. Time dependence of the half-chain von Neumann entanglement entropy for the XXZ chain with even $n \geq 4$ at various values of the anisotropy parameter Δ with $J = 1$. All curves are plots of the analytical results using Eq. (34).

where the prefactor 2 reflects the doubled number of contributing dimers for $n > 2$, and the factor $1/2$ in the time dependence reflects the fact that only one postquench coupling is involved in each pair of dimers.

From Eq. (34), the von Neumann EE for an even $n > 2$ chain is explicitly given by

$$\begin{aligned}
 S_1^{n=\text{even}}(t) &= 4 - \sin^2(Jt/2) \log_2 \sin^2(Jt/2) \\
 &\quad - \frac{1}{2} [1 + \cos^2(Jt/2) + 2 \cos(Jt/2) \cos(J\Delta t/2)] \\
 &\quad \times \log_2 [1 + \cos^2(Jt/2) + 2 \cos(Jt/2) \cos(J\Delta t/2)] \\
 &\quad - \frac{1}{2} [1 + \cos^2(Jt/2) - 2 \cos(Jt/2) \cos(J\Delta t/2)] \\
 &\quad \times \log_2 [1 + \cos^2(Jt/2) - 2 \cos(Jt/2) \cos(J\Delta t/2)], \quad (35)
 \end{aligned}$$

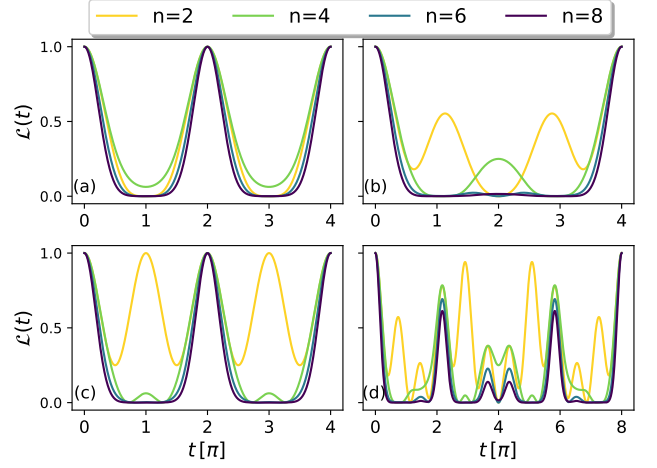


FIG. 4. Time dependence of the exact Loschmidt echo for the XXZ chain of length $N = 2n$, $n = 2, 4, 6$ and 8 with $J = 1$ and various values of the anisotropy parameter: (a) $\Delta = 0$, corresponding to the XX chain; (b) $\Delta = 1/2$; (c) $\Delta = 1$, the XXX chain; (d) $\Delta = 7/4$.

and the Rényi EE is

$$\begin{aligned}
 S_2^{n=\text{even}}(t) &= 6 - 2 \log_2 [1 + \sin^4(Jt/2) + 2 \cos^2(Jt/2) \\
 &\quad + \cos^4(Jt/2) + 4 \cos^2(Jt/2) \cos^2(J\Delta t/2)]. \quad (36)
 \end{aligned}$$

For $n = 4$, the analytical forms of the eigenvalues of the 16 reduced density matrices for the XX- and XXX-chains are provided in Appendix A.

We note that the dynamical entanglement entropy is a periodic function of time, with a period $2q\pi$ for $n > 2$ and $q\pi$ for $n = 2$, provided $\delta \equiv J\Delta = p/q$ with p and q being coprime integers. To illustrate this, we plot in Fig. 3 the time-dependent entanglement entropy for chains with even $n > 2$ and with various values of the anisotropy parameter Δ by fixing $J = 1$. The case for the golden mean values $\Delta = \tau$ and $\Delta = 1/\tau$ with $\tau = (\sqrt{5} + 1)/2$, shown in Fig. 3(d), displays no periodicity.

B. Loschmidt echo

Given the $2n$ -site initial state and the time-evolved state in the Bell representation [Eq. (12)], the Loschmidt echo, defined as the overlap of both states, can be rewritten as

$$\begin{aligned}
 \mathcal{L}(t) &= \left| \sum_{k \in k^*} a_k^2 \exp(-iE_k t) \right|^2 \\
 &= \left| \frac{1}{4^{n-1}} \sum_{k \in k^*} \exp(-iE_k t) \right|^2, \quad (37)
 \end{aligned}$$

where the nonzero coefficients a_k satisfy the selection rules given in Sec. II A, and the energy E_k of k -th state is just the sum of the energies of participating Bell dimers [Eq. (10)].

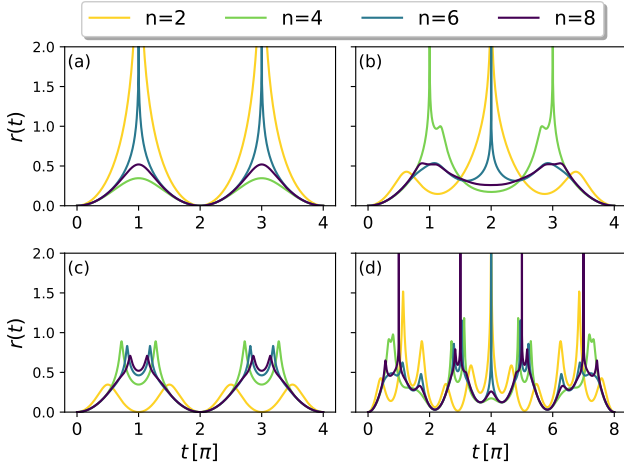


FIG. 5. Time dependence of the return rate function calculated from the Loschmidt echo in Fig. 4 for the XXZ chain with $J = 1$ and the anisotropy parameter at (a) $\Delta = 0$, corresponding to the XX chain; (b) $\Delta = 1/2$; (c) $\Delta = 1$, the XXX chain; (d) $\Delta = 7/4$.

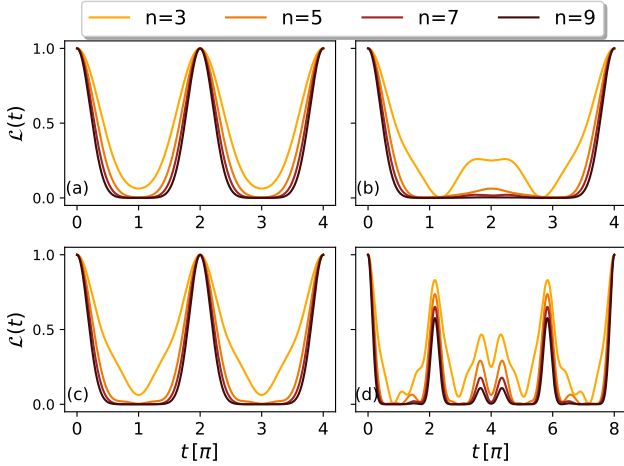


FIG. 6. Time dependence of the exact Loschmidt echo for the XXZ chain with odd $n = 3, 5, 7, 9$ and at various values of the anisotropy parameter: (a) $\Delta = 0$, corresponding to the XX chain; (b) $\Delta = 1/2$; (c) $\Delta = 1$, the XXX chain; (d) $\Delta = 7/4$. All curves are plotted with fixed $J = 1$.

Below we present closed-form solutions of short XXZ chains with $n = 2, 3, 4, 6$ and XX chains up to $n = 8$. For the shortest chain with $n = 2$, the dimer configurations for nonzero coefficients are given in Eq. (23), leading to the Loschmidt echo

$$\begin{aligned} \mathcal{L}^{n=2}(t) &= \frac{1}{16} |e^+ + 2e^0 + e^-|^2 \\ &= \frac{1}{4} [1 + 2 \cos(Jt) \cos(\Delta Jt) + \cos^2(Jt)] \end{aligned} \quad (38)$$

where the same shorthand notations as in Eq. (24) are used.

For the $n = 3$ chain with 16 nonzero a_k , the analytical

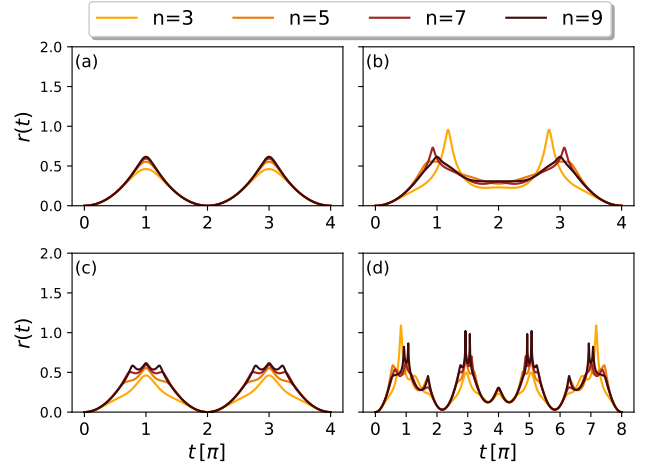


FIG. 7. Time dependence of the return rate function calculated from the Loschmidt echo in Fig. 6 for the XXZ chain with $J = 1$ and the anisotropy parameter at (a) $\Delta = 0$, corresponding to the XX chain; (b) $\Delta = 1/2$; (c) $\Delta = 1$, the XXX chain; (d) $\Delta = 7/4$.

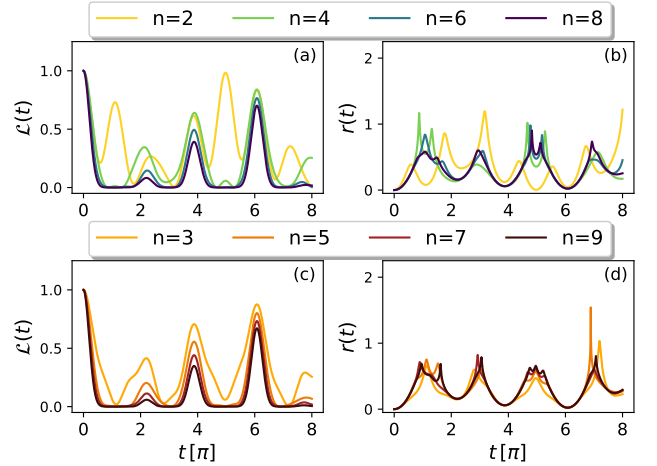


FIG. 8. Time dependence of the Loschmidt echo [(a) and (c)] and the return rate function [(b) and (d)] with an irrational value of the anisotropy parameter $\Delta = 2/(\sqrt{5} + 1)$ for the XXZ chain of length $2n$ with even n [upper panel (a) and (b)] and odd n [lower panel (c) and (d)]. The coupling strength is fixed at $J = 1$.

result for Loschmidt echo is

$$\begin{aligned} \mathcal{L}^{n=3}(t) &= \frac{1}{256} \{36 \cos(\Delta Jt) + 36 \cos[(1 - \Delta)Jt] + \\ &\quad + 12 \cos[(1 + \Delta)Jt] + 72 \cos(Jt) \\ &\quad + 6 \cos(2Jt) + 12 \cos[(2 + \Delta)Jt] + 82\} . \end{aligned} \quad (39)$$

For the chain with $n = 4$, we obtain

$$\begin{aligned} \mathcal{L}^{n=4}(t) &= \frac{1}{256} \left\{ [12 \cos^2(Jt/2) + \cos(J\Delta t) (3 + \cos^2(Jt))]^2 \right. \\ &\quad \left. + \sin^2(J\Delta t) \sin^4(Jt) \right\} . \end{aligned} \quad (40)$$

An analytical expression for $n = 6$ with arbitrary values of Δ is given in Appendix B.

For the special case $\Delta = 0$ (XX chain), we have

$$\mathcal{L}_{XX}^{n=2}(t) = \frac{1}{4} [1 + \cos(Jt)]^2, \quad (41)$$

$$\mathcal{L}_{XX}^{n=4}(t) = \frac{1}{4^5} [19 + 12 \cos(Jt) + \cos(2Jt)]^2, \quad (42)$$

$$\mathcal{L}_{XX}^{n=6}(t) = \frac{1}{4^9} [226 + 255 \cos(Jt) + 30 \cos(2Jt) + \cos(3Jt)]^2, \quad (43)$$

$$\mathcal{L}_{XX}^{n=8}(t) = \frac{1}{4^{13}} [3225 + 3976 \cos(Jt) + 924 \cos(2Jt) + 56 \cos(3Jt) + \cos(4Jt)]^2, \quad (44)$$

where the Loschmidt echo for even n is written as a quadratic form in a superposition of $\cos(\mu Jt)$ -terms with $\mu = 0, 1, \dots, n/2$ and a global prefactor $C_n = 1/4^{2n-3}$. Similarly, for odd n , it can be written as linear combination of $\cos(\mu Jt)$ -terms with $\mu = 0, 1, \dots, n-1$ and $C_n = 1/4^{2n-2}$. Explicit expressions for odd $n = 5, 7$ and 9 are provided in Appendix C. Extensions to larger n are straightforward. These expressions also imply that the corresponding Loschmidt amplitude, $\langle \Psi_0 | \Psi_0(t) \rangle$, is real for even n and is complex for odd n .

In Fig. 4-8 we plot the Loschmidt echo $\mathcal{L}(t)$ and the return rate function $r(t)$ (defined in Eq. (20)) as functions of time for various chain lengths and five values of the anisotropy parameter, with fixed $J = 1$. Consistent with the dynamical entanglement entropy, the Loschmidt echo for $n > 2$ is a periodic function of time with a period of $2q\pi$, provided $J\Delta = p/q$ with p and q being coprime integers. For the shortest chain, $n = 2$, the period deviates from this rule in some cases, such as when $\Delta = 1$, where the period is π [Fig. 4(c)]. For an irrational value of Δ , the Loschmidt echo is non-periodic, as illustrated in Fig. 8 for $\Delta = 1/\tau$ with $\tau = (\sqrt{5} + 1)/2$.

Moreover, we observe exact zeros of the Loschmidt echo for even n . For instance, the XX chain ($\Delta = 0$) with $n = 2$ has Loschmidt zeros at $t = \pi, 3\pi, \dots$; the $n = 4$ XXZ chain with $\Delta = 1/2$, and also the longer $n = 8$ chain with $\Delta = 7/4$ exhibit zeros at $t = \pi, 3\pi, \dots$, too. At these instances, the return rate function becomes divergent, as shown in Fig. 5. In all cases considered here, Loschmidt zeros do not appear in odd n chains [Fig. 6 and 7], nor in the XXX chain for any n . For the irrational value $\Delta = 2/(\sqrt{5} + 1)$, we find no Loschmidt zeros up to $t = 8\pi$ [see Fig. 8 (b) and (d)].

C. Dynamical quantum phase transitions and finite-size scaling

Since the prequench and postquench Hamiltonians belong to distinct topological phases, the quench considered here is expected to exhibit dynamical phase transitions [59, 64].

Under a fermionic transformation, the XX chain decouples into two transverse-field Ising chains [65, 66]. Within this mapping, the present protocol by assuming $J = 1$ then corresponds to a quench from a fully polarized initial state along the transverse-field direction, $|\Psi_0\rangle = \bigotimes_i |\rightarrow_i\rangle$, evolved under a classical Ising Hamiltonian. Equivalently, it can be

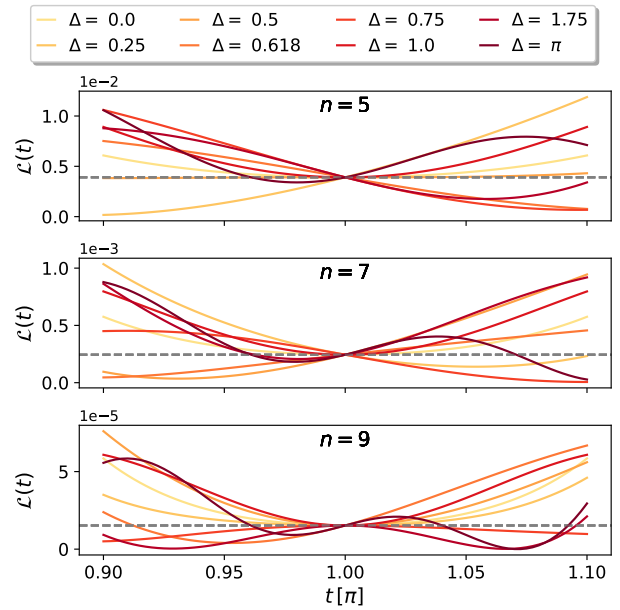


FIG. 9. Visualization of the Loschmidt echo for the XXZ chain with odd $n = 5, 7, 9$ and various values of Δ , where the label $\Delta = 0.618$ indicates an irrational value $\Delta = 2/(\sqrt{5} + 1)$. At $t = \pi$, all the curves intersect exactly at $(1/2)^{2(n-1)}$ (dashed line). The coupling strength is fixed at $J = 1$.

viewed as a quench from a fully polarized state into a cluster phase [67] governed by $\mathcal{H}_{\text{cluster}} = -1/4 \sum_i Z_{i-1} X_i Z_{i+1}$, where X and Z denote Pauli matrices. Previous studies [68] have established that such quenches exhibit dynamical quantum phase transitions at critical times $t^* = (2m + 1)\pi$, with $m = 0, 1, 2, \dots$.

Based on the exact results obtained here, we identify distinct finite-size scaling behaviors of the Loschmidt echo \mathcal{L}^* and the return rate function r^* at t^* in the finite XX chain:

Case (i): For $n = 4\nu + 2, \nu = 0, 1, 2, \dots$:

$$\mathcal{L}_{XX}^* = 0, \quad r^* = \infty.$$

Case (ii): For $n = 4\nu + 4, \nu = 0, 1, 2, \dots$:

$$\mathcal{L}_{XX}^* = (1/2)^{2(n-2)}, \quad r^* = (1 - 2/n) \ln 2.$$

Case (iii): For odd n :

$$\mathcal{L}_{XX}^* = (1/2)^{2(n-1)}, \quad r^* = (1 - 1/n) \ln 2.$$

In Cases (ii) and (iii), \mathcal{L}^* and r^* converge monotonically to $\mathcal{L}^* = 0$ and $r^* = \ln 2$ as n increases, whereas in Case (i) exact Loschmidt zeros occur at special even n .

Remarkably, for odd n , the finite-size scaling of \mathcal{L} and r at $t = (2m + 1)\pi$ holds for arbitrary values of the anisotropy parameter Δ . For instance, at $n = 3$, Eq. (39) yields $\mathcal{L}^{n=3}(t) = 1/16$ at odd multiples of π for any $\Delta \in \mathbb{R}$. Figure 9 displays the Loschmidt echo for chain lengths $n = 5, 7, 9$ and various

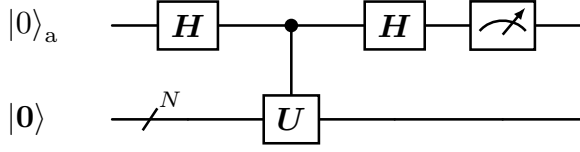


FIG. 10. Hadamard test circuit for computing the real part of the expectation value $\text{Re}(\langle \mathbf{0} | U | \mathbf{0} \rangle)$, where $|\mathbf{0}\rangle = |0\rangle^{\otimes N}$ is an N -qubit state and $|0\rangle_a$ is the initial state of an ancilla qubit.

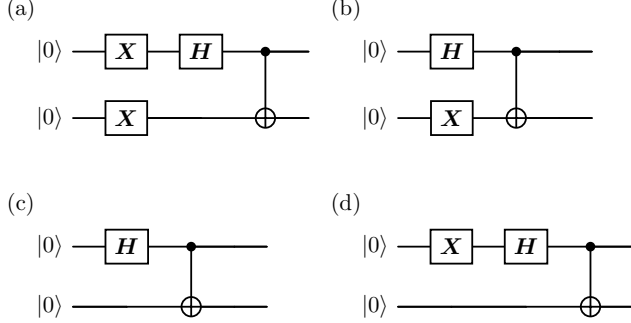


FIG. 11. Quantum circuits to generate four Bell states: (a) $|\psi_0\rangle = (|01\rangle - |10\rangle)/\sqrt{2}$; (b) $|\psi_1\rangle = (|01\rangle + |10\rangle)/\sqrt{2}$; (c) $|\psi_2\rangle = (|00\rangle + |11\rangle)/\sqrt{2}$; (d) $|\psi_3\rangle = (|00\rangle - |11\rangle)/\sqrt{2}$.

Δ , including irrational values, showing a universal crossing at $t = \pi$ with $\mathcal{L} = (1/2)^{2(n-1)}$.

These results indicate that quenches in the flat-band limit of the XXZ chain exhibit dynamical phase transitions at $t^* = (2m + 1)\pi$, independent of Δ , where $-\ln \mathcal{L}_{XXZ}(t^*) \rightarrow \infty$ and $r(t^*) \rightarrow \ln 2$ in the thermodynamic limit. For certain finite system sizes with even n , additional exact zeros of \mathcal{L}_{XXZ} occur at times $t \neq t^*$, for example at even multiples of π [see Fig. 5].

A further noteworthy feature is that the dynamical phase transitions considered here are also characterized by maximum entanglement entropy for $n > 2$. At the critical times $t^* = (2m + 1)\pi$ with $J = 1$, the entanglement entropy reaches $S = 4$ for even $n > 2$ and $S = 3$ for odd n , independent of Δ , as can be verified from Eqs. (33) and (34).

IV. DIGITAL QUANTUM SIMULATION

In this section we present the relevant setups for our simulations using the IBM Quantum Platform, and show simulation results for time-dependent entanglement entropies and the Loschmidt echo.

The simulation data presented here were obtained from the quantum device *ibm.fez*, a 156 qubit-system of type Heron, and a few from a noisy simulator based on the real device.

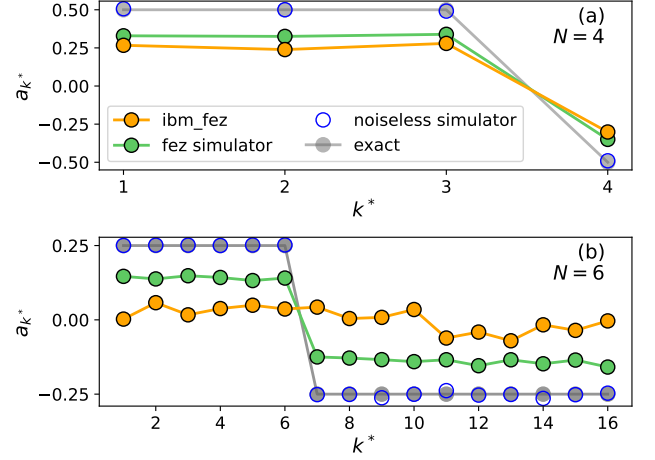


FIG. 12. Nonzero amplitudes $a_k = \langle \Phi_k | \Psi_0 \rangle$, $k \in k^*$ for chain lengths $N = 4$ (a) and $N = 6$ (b), estimated using the Hadamard test on the IBM quantum device *ibm.fez* and its noisy simulator, compared with results from noiseless simulations and exact solutions.

A. Hadamard test for a_k estimation

Our first numerical experiment estimates the coefficients (amplitudes) $a_k = \langle \Phi_k | \Psi_0 \rangle$ using the Hadamard test [39]. The Hadamard test circuit, shown in Fig. 10, consists of two Hadamard gates H acting on a single ancilla qubit, which serves as the control qubit for a controlled- U gate. The unitary is defined as $U = U_{\Phi_k}^\dagger U_{\Psi_0}$, where U_{Ψ_0} and U_{Φ_k} generate the states $|\Psi_0\rangle$ and $|\Phi_k\rangle$, respectively, from a register of N qubits initialized to $|\mathbf{0}\rangle = |0\rangle^{\otimes N}$:

$$|\Psi_0\rangle = U_{\Psi_0} |\mathbf{0}\rangle, \quad |\Phi_k\rangle = U_{\Phi_k} |\mathbf{0}\rangle. \quad (45)$$

Since $|\Psi_0\rangle$ and $|\Phi_k\rangle$, are both product states of Bell states, they can be constructed via tensor products of following unitaries [Fig. 11]:

$$U_{\psi_0} = C_X (H \otimes I) (X \otimes X) \quad (46)$$

$$U_{\psi_1} = C_X (H \otimes X) \quad (47)$$

$$U_{\psi_2} = C_X (H \otimes I) \quad (48)$$

$$U_{\psi_3} = C_X (H \otimes I) (X \otimes I), \quad (49)$$

where C_X denotes the CNOT gate, X the Pauli- X gate, and I represents the identity operator.

To implement the controlled- U gate, we first construct the circuits preparing $|\Psi_0\rangle$ and $|\Phi_k\rangle$ and convert them into unitary operators using the `to_gate()` function in Qiskit [69]. We then form $U = U_{\Phi_k}^\dagger U_{\Psi_0}$ and convert it to a controlled operation,

$$C_U = \begin{pmatrix} I & 0 \\ 0 & U \end{pmatrix}, \quad (50)$$

using `ControlledGate`, with an ancilla qubit as the control qubit initialized by a Hadamard gate.

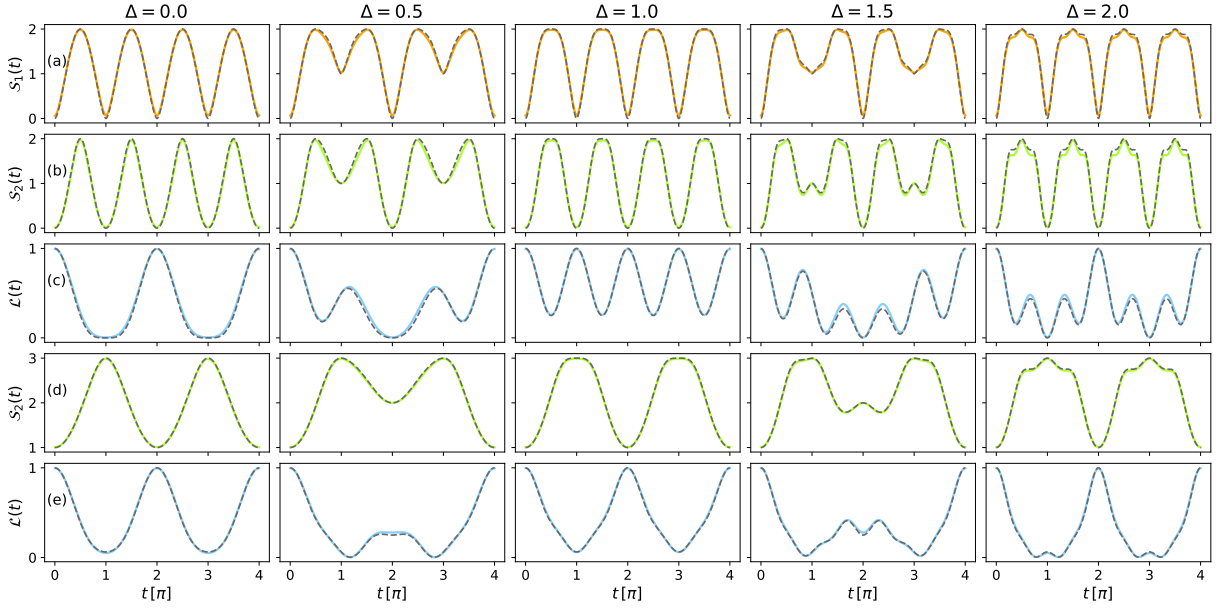


FIG. 13. Simulation results (solid lines) for the half-chain entanglement entropies and the Loschmidt echo for a chain of length $N = 4$ [Panel (a) - (c)] and $N = 6$ [Panel (d) and (e)] at various parameter Δ , compared with exact solutions (dashed lines). The simulation data are based on the normalized coefficients a_k , estimated using the Hadamard test on the quantum device *ibm_fez* for $N = 4$ and on the noisy *ibm* simulator for $N = 6$.

The ancilla qubit is measured in the Z basis after a second Hadamard gate. The probabilities of measuring 0 and 1 in the ancilla qubit are

$$\begin{aligned} P_0 &= \frac{1}{4} (2 + \langle \mathbf{0} | \mathbf{U} + \mathbf{U}^\dagger | \mathbf{0} \rangle), \\ P_1 &= \frac{1}{4} (2 - \langle \mathbf{0} | \mathbf{U} + \mathbf{U}^\dagger | \mathbf{0} \rangle). \end{aligned} \quad (51)$$

Thus, we obtain the coefficient $a_k \in \mathbb{R}$, the real part of the amplitude, by

$$a_k = \text{Re} [\langle \mathbf{0} | \mathbf{U} | \mathbf{0} \rangle] = P_0 - P_1. \quad (52)$$

Based on the selection rules described in Sec. II A, we apply the Hadamard test exclusively to those active states $|\Phi_{k^*}\rangle$ that yield nonzero a_{k^*} . Results for $N = 4$ and $N = 6$, simulated on the IBM device *ibm_fez* and its noisy simulator, are shown in Fig. 12. For each data point, $N_M = 2^{13}$ measurements for $N = 4$ and $N_M = 2^{14}$ for $N = 6$ were performed. For $N = 4$, only four active states contribute to the superposition: three with positive coefficients and one with a negative coefficient. The Hadamard test correctly reproduces the signs of these coefficients, though the measured magnitudes are systematically smaller than the exact values. For $N = 6$, the number of active states increases to 16, and the accuracy of results from the real device declines significantly. This accuracy decline stems from two factors: the rapidly increasing circuit depth (exceeding 300 for $N = 6$) and the decreasing amplitude magnitudes ($|a_{k^*}| = 0.25$ for $N = 6$) for longer chains.

We constructed the time-evolved state $|\Psi_0(t)\rangle$ using these estimated amplitudes and renormalized them according to the

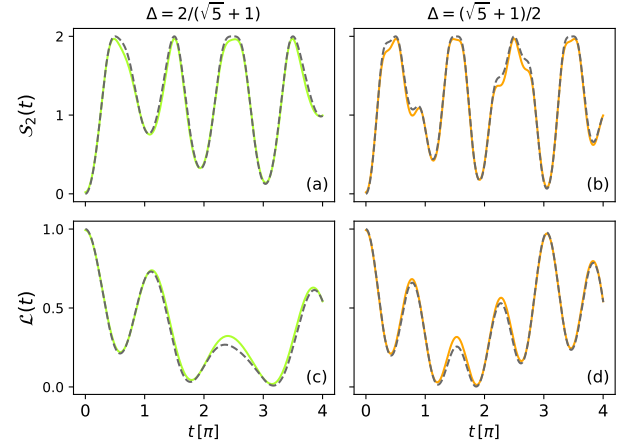


FIG. 14. Simulation results (solid lines) for the half-chain Rényi entanglement entropy and the Loschmidt echo for a chain of $N = 4$ with $\Delta = 2/(\sqrt{5} + 1)$ and $\Delta = (\sqrt{5} + 1)/2$. The simulation data are based on the normalized coefficients a_k , estimated using the Hadamard test on *ibm_fez*.

condition:

$$a_{k^*} \leftarrow \frac{a_{k^*}}{\sqrt{\sum_{k^*} a_{k^*}^2}} \quad (53)$$

This normalization procedure serves as an error mitigation strategy since the exact coefficients a_{k^*} inherently satisfy this normalization condition. With the time-evolved state constructed, we then calculated the observables of interest, including the von Neumann entanglement entropy of a half chain, the Rényi entanglement entropy, and the Loschmidt

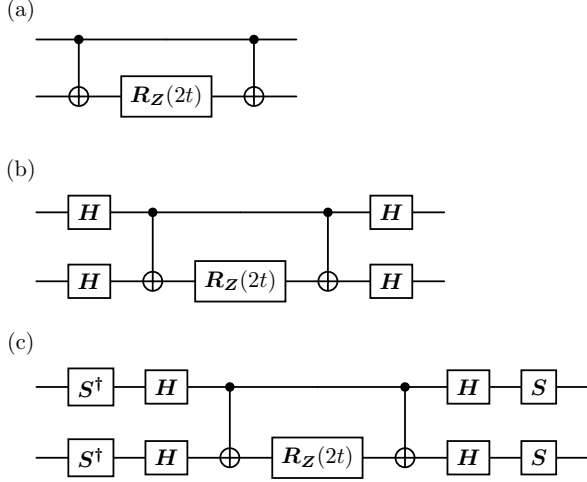


FIG. 15. Quantum circuits to implement the time-evolution operators: (a) $\exp(-itZZ)$; (b) $\exp(-itXX)$; (c) $\exp(-itYY)$.

echo.

Figure 13 [panel (a)-(c)] presents the observable measurements for $N = 4$ obtained using the normalized amplitudes a_k from the Hadamard test on the IBM device *ibm_fez*. For $N = 6$, however, the inaccurate coefficients estimated from the real device produce physically meaningless results for the observables. Consequently, we employed coefficients obtained from the noisy simulator to calculate the observables shown in Fig. 13 (d) and (e).

The entanglement entropy and the Loschmidt echo produced by the estimated amplitudes from *ibm_fez* for the $N = 4$ chain with an irrational $\Delta = 2/(\sqrt{5} + 1)$ are presented in Fig. 14. The data are also in good agreement with the exact solutions.

B. Time evolution circuit

While the Hadamard test enables direct amplitude estimation of time-evolved states in the Bell basis, it yields accurate results only for very small systems on real quantum devices. As system size grows, circuit depth increases substantially, degrading accuracy on noisy hardware. Error mitigation techniques, such as readout error mitigation, zero-noise extrapolation, and Pauli twirling, can partially compensate for hardware noise [70]; however, the exponential decay of amplitude magnitudes with system size ultimately limits the practical scalability of this approach in our simulations.

A more scalable approach is to construct time-evolved states by applying time-evolution operators to the initial state. The key challenge is designing shallow circuits for time evolution that avoid substantial Trotter errors [71]. For the fully dimerized model considered here, this challenge is resolved: the time-evolution circuit $U(t) = \exp(-i\mathcal{H}_2t)$ is Trotter-error-free for any anisotropy parameter Δ and arbitrary time duration t , with circuit depth remaining constant as t increases.

The time evolution operator governed by \mathcal{H}_2 can be decomposed as

$$U(t, \Delta) = \bigotimes_j U_{2j}(t, \Delta), \quad (54)$$

with

$$\begin{aligned} U_{2j}(t, \Delta) &= \exp\left[-\frac{it}{4}(\mathbf{X}_{2j}\mathbf{X}_{2j+1} + \mathbf{Y}_{2j}\mathbf{Y}_{2j+1} + \Delta\mathbf{Z}_{2j}\mathbf{Z}_{2j+1})\right] \\ &= \exp\left(-\frac{it}{4}\mathbf{X}_{2j}\mathbf{X}_{2j+1}\right)\exp\left(-\frac{it}{4}\mathbf{Y}_{2j}\mathbf{Y}_{2j+1}\right) \\ &\quad \exp\left(-\frac{it}{4}\Delta\mathbf{Z}_{2j}\mathbf{Z}_{2j+1}\right), \end{aligned} \quad (55)$$

in terms of Pauli gates \mathbf{X} , \mathbf{Y} and \mathbf{Z} . The quantum circuits implementing the three exponential operators with ZZ , XX , and YY couplings are illustrated in Fig. 15(a), 15(b), and 15(c), respectively. In this setup, the exponential operators are related to each other through the basis transformation: $(\mathbf{u}^X)^\dagger \mathbf{Z} \mathbf{u}^X = \mathbf{X}$ and $(\mathbf{u}^Y)^\dagger \mathbf{Z} \mathbf{u}^Y = \mathbf{Y}$ with $\mathbf{u}^X = \mathbf{H}$ and $\mathbf{u}^Y = \mathbf{H}\mathbf{S}^\dagger$, where \mathbf{S} is a phase shift gate which rotates a state vector a $\pi/2$ radian around the Z -axis.

C. Randomized measurements

To extract the second-order Rényi entanglement entropy and Loschmidt echo from the time-evolved quantum state prepared by the time-evolution circuit, we employ a random Pauli measurement scheme, in which each qubit is measured in a randomly chosen X , Y or Z basis [43, 44]. The local random unitaries used to rotate the measurement basis can be sampled from the single-qubit Clifford ensemble.

The measurement protocol proceeds as follows: (i) Prepare the postquench state $\rho(t)$ of N qubits at time t using the time-evolution circuit. (ii) Apply a random unitary transformation, $\rho \rightarrow \mathbf{U}\rho\mathbf{U}^\dagger$, where $\mathbf{U} = \bigotimes_{i=1}^N \mathbf{u}_i$ and each \mathbf{u}_i is randomly drawn from $\{\mathbf{H}, \mathbf{H}\mathbf{S}^\dagger, \mathbf{I}\}$, thereby rotating the local measurement basis to a randomly chosen Pauli basis $\{X, Y, Z\}$. (iii) Measure each qubit in the standard Z basis, obtaining a bitstring $\mathbf{b} = z_1 \cdots z_N$ with $z_i = 0, 1$. For each fixed unitary \mathbf{U} , the measurement is repeated N_M times. The full procedure is then repeated for N_U independently sampled unitaries. The resulting $N_U \times N_M$ bitstrings and corresponding sets of single-qubit unitaries are stored for classical post-processing.

We apply two post-processing protocols to estimate the second-order Rényi entanglement entropy (EE) and the Loschmidt echo. In the first protocol, the purity of a subsystem A , required for the Rényi EE, is estimated from statistical correlations of randomized measurements via [40–42]:

$$\text{Tr}[\rho_A^2] = \frac{2^{N_A}}{N_U} \sum_{\mathbf{U}} \sum_{\mathbf{b}_A, \mathbf{b}'_A} (-2)^{-D[\mathbf{b}_A, \mathbf{b}'_A]} P_{\mathbf{U}}(\mathbf{b}_A) P_{\mathbf{U}}(\mathbf{b}'_A), \quad (56)$$

where $D[\mathbf{b}_A, \mathbf{b}'_A] \equiv |\{i \in A | z_i \neq z'_i\}|$ is the Hamming distance between two bitstrings $\mathbf{b}_A = z_1 \cdots z_{N_A}$ and $\mathbf{b}'_A = z'_1 \cdots z'_{N_A}$, and $P_{\mathbf{U}}(\mathbf{b}_A)$ denotes the probability of measuring

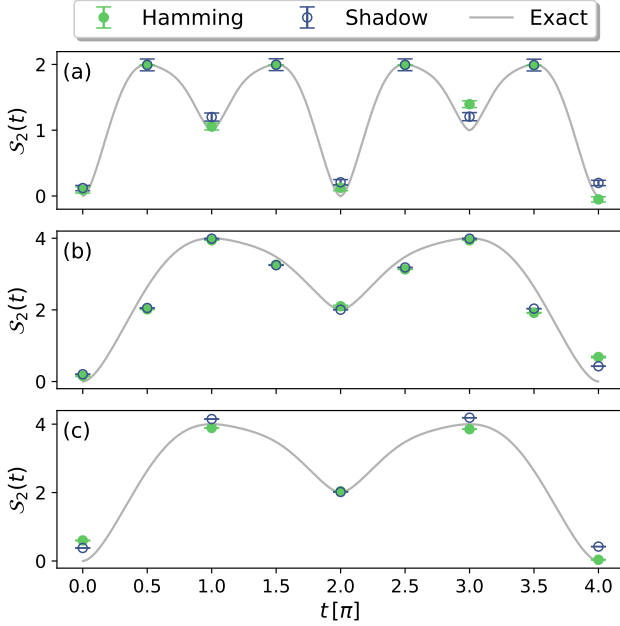


FIG. 16. Results of random Pauli measurements for dynamical half-chain Rényi entanglement entropy of the XXZ chain with $\Delta = 0.5$ and with $N = 4$ (a), $N = 8$ (b), and $N = 12$ (c) sites. The same measurement outcomes are analyzed using Hamming distance method [Eq. (56)] and classical shadow technique [Eq. (59)], and compared with the exact solutions (solid lines). For $N = 8$, we consider the subsystem consisting of the four bulk qubits in the open chain, while for $N = 4$ and $N = 12$ the subsystems consist of $N/2$ adjacent qubits in a chain with PBC.

bitstring \mathbf{b}_A under unitary U . Similarly, the overlap between two N -qubit states ρ_1 and ρ_2 can be estimated using [42]:

$$\text{Tr}[\rho_1 \rho_2] = \frac{2^N}{N_U} \sum_U \sum_{\mathbf{b}, \mathbf{b}'} (-2)^{-D[\mathbf{b}, \mathbf{b}']} P_U^{(1)}(\mathbf{b}) P_U^{(2)}(\mathbf{b}'), \quad (57)$$

where $P_U^{(1)}$ and $P_U^{(2)}$ are the probabilities based on ρ_1 and ρ_2 , respectively. From the subsystem purity, we compute the Rényi EE of a half-chain, while identifying $\rho_1 = \rho(0) = |\Psi_0\rangle \langle \Psi_0|$ and $\rho_2 = \rho(t)$ yields the Loschmidt echo.

A second post-processing protocol employs the pairs of random unitaries and measurement outcomes, $\{(U, \mathbf{b})\}$, to construct classical shadows of the quantum state [43, 44]. If $|\mathbf{b}\rangle = |z_1 \cdots z_N\rangle$ is the measurement outcome in the Z basis after applying the unitary transformation $U = \bigotimes_{i=1}^N \mathbf{u}_i$ to an N -qubit state ρ , a classical snapshot of the state can be constructed as $\bigotimes_{i=1}^N \mathbf{u}_i^\dagger |z_i\rangle \langle z_i| \mathbf{u}_i$. The reduced state on a subsystem A is then reconstructed via inverting an N_A -qubit depolarizing channel [43, 44]:

$$\hat{\rho}_A = \bigotimes_{i \in A} \left[3\mathbf{u}_i^\dagger |z_i\rangle \langle z_i| \mathbf{u}_i - \mathbf{I} \right]. \quad (58)$$

The collection of inverted snapshots, $\{\hat{\rho}^{(m)}\}_{m=1}^M$, obtained over M measurements, constitutes the classical shadow of the

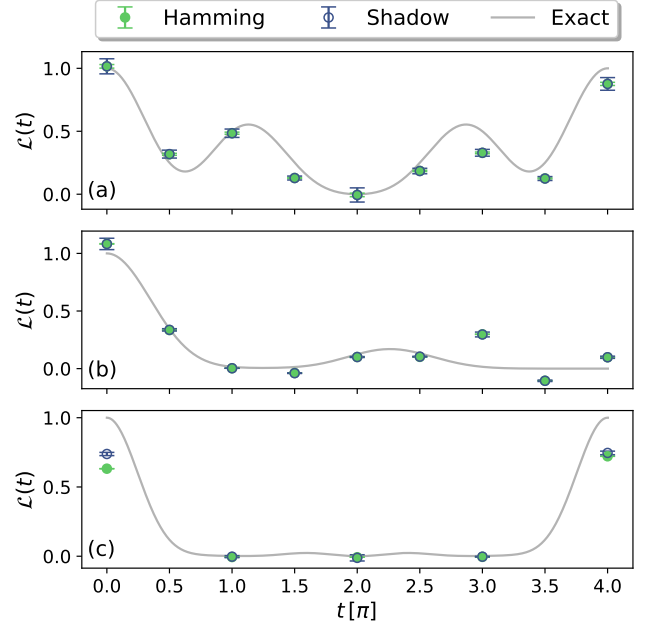


FIG. 17. Results of random Pauli measurements for the Loschmidt echo in the XXZ chain with $\Delta = 0.5$ and with $N = 4$ (a), $N = 8$ (b), and $N = 12$ (c) sites. For $N = 8$, the system has open boundary conditions, while for $N = 4$ and $N = 12$, periodic boundary conditions are considered. The results were evaluated using the same measurement data as in Fig. 16.

state. In our implementation, the classical shadows are built using the same measurement data as in the first protocol based on weighted averages of Hamming distances [see Eq. (56)]. That is, we have $M = N_U \times N_M$.

In this protocol, the subsystem purity is estimated as an average over all pairs of shadows [43, 44]:

$$\text{Tr}[\rho_A^2] = \frac{1}{M(M-1)} \sum_{m \neq m'} \text{Tr}[\hat{\rho}_A^{(m)} \hat{\rho}_A^{(m')}], \quad (59)$$

for $m, m' = 1, \dots, M$. We have used the following identity to efficiently compute the trace of the product:

$$\text{Tr}[\mathbf{A}\mathbf{B}] = \prod_i \text{Tr}[\mathbf{A}_i \mathbf{B}_i], \quad \mathbf{A} = \bigotimes_i \mathbf{A}_i, \quad \mathbf{B} = \bigotimes_i \mathbf{B}_i. \quad (60)$$

Denoting a local shadow by $\sigma_z^\alpha = 3\mathbf{u}^{\alpha\dagger} |z\rangle \langle z| \mathbf{u}^\alpha - \mathbf{I}$, with one of the three possible unitaries \mathbf{u}^α corresponding to measurement bases $\alpha \in \{X, Y, Z\}$ and two possible outcomes $z \in \{0, 1\}$, the three possible trace values for a local shadow pair are given by

$$\text{Tr}[\sigma_z^\alpha \sigma_{z'}^{\alpha'}] = \begin{cases} 5 & \text{if } \alpha = \alpha', z = z' \\ -4 & \text{if } \alpha = \alpha', z \neq z' \\ 1/2 & \text{if } \alpha \neq \alpha'. \end{cases} \quad (61)$$

This rule, together with the identity in Eq. (60), provides an efficient and scalable method for evaluating the purity using

the classical shadow formalism. This method has been incorporated into a software package for sampling and post-processing randomized measurements [72].

To obtain the Loschmidt echo, we first estimate the N -qubit state for a given set of random unitaries $U = \bigotimes_{i=1}^N u_i$ at time t by averaging over N_M measurement outcomes:

$$\hat{\rho}^U(t) = \frac{1}{N_M} \sum_{j=1}^{N_M} \bigotimes_{i=1}^N \left[3u_i^\dagger |z_i\rangle \langle z_i| u_i - \mathbf{I} \right]. \quad (62)$$

We then use the exact density matrix $\rho(0) = |\Psi_0\rangle \langle \Psi_0|$ of the initial state $|\Psi_0\rangle$ to evaluate the Loschmidt echo via the ensemble average of the overlap:

$$\mathcal{L}(t) = \frac{1}{N_U} \sum_U \text{Tr} [\rho(0) \hat{\rho}^U(t)] \quad (63)$$

In Fig. 16 and Fig. 17, we present the results for the half-chain Rényi EE and the Loschmidt echo, respectively, comparing data obtained from random Pauli measurements with the exact solutions. The same measurement data are post-processed using Hamming distance method and classical shadow technique. According to previous studies [40, 42–44], for a fixed total number $M = N_M \times N_U$, the Hamming distance method yields more accurate estimates when the number of measurement shots N_M is large, whereas the classical shadow technique performs better when N_U is large. Without optimizing the ratio of N_M and N_U for our setting, we chose $N_U = 2^6$ and $N_M = 2^{13}$.

We consider systems with $\Delta = 0.5$ and $N = 4, 8$, and 12 qubits. For $N = 4$ and $N = 12$, periodic boundary conditions (PBC) were implemented, which require connectivity between the first and last qubits, typically achieved through ancilla qubits and additional gates. For the $N = 12$ system, we utilized the heavy-hexagon lattice structure of the IBM quantum processors to select a ring of qubits along the hexagonal arrangement, allowing PBC to be realized without extra gates or ancillas [13]. For $N = 8$, we simulated a chain with OBC to keep the circuit depth shallow for this system size.

Without any error mitigation, the simulated half-chain EE shows overall good agreement with the exact results. For the Loschmidt echo, where the full system contributes, some noticeable deviations from the exact solutions appear at certain times. Nonetheless, the results from the two post-processing methods agree well with each other across all cases studied.

V. SUMMARY AND DISCUSSION

We have analytically and numerically investigated quantum quenches in the XXZ chain with alternating interactions in the flat-band limit. The quench protocol we considered interchanges the odd- and even-bond strengths of an initially fully dimerized chain. By formulating the problem in the Bell basis, we established selection rules identifying all Bell states with nonzero expansion coefficients in the time-dependent state for arbitrary even system sizes. For a chain of length N , all nonzero coefficients have equal magnitude $|a_k| = 2^{-(N/2-1)}$.

We further derived exact relations connecting the dynamical half-chain entanglement entropies of the $N = 4$ system to those of any even system with $N > 4$. We also derived a series of closed-form solutions for the Loschmidt echo up to $N = 12$, which can be extended to numerically exact results for arbitrary N using the exact coefficients $|a_k|$.

From these exact results, we identified distinct finite-size scaling behaviors of the Loschmidt echo \mathcal{L}^* in the XX chain at critical times, depending on the chain length $N = 2n$. For odd n , the scaling, $\mathcal{L}^* = (1/2)^{2(n-1)}$, is found to hold for arbitrary values of the anisotropy parameter $\Delta \in \mathbb{R}$, revealing universal behavior at the dynamical phase transitions in the flat-band limit of the XXZ chain. Extending the analysis to $N \leq 18$, we identified a sequence of Loschmidt zeros occurring in specific finite chains. No such zeros appear in the isotropic XXX case ($\Delta = 1$). Both the entanglement entropy and the Loschmidt echo exhibit persistent oscillations, reflecting the absence of relaxation in this flat-band system. For $N > 4$, these observables are periodic with period $2q\pi$ when $J\Delta = p/q$ is an irreducible fraction.

On the digital quantum simulation side, we performed two complementary experiments on IBM-Q devices. First, we used the Hadamard test to evaluate scalar products between the initial state $|\Psi_0\rangle$ and Bell basis vectors $|\Phi_k\rangle$, including their phase (sign) information. Combined with the known energies of the Bell states, this enabled us to reconstruct the time-dependent state in the Bell basis and compute dynamical observables. Using the normalization condition as a simple error mitigation strategy, this approach produces accurate results for $N = 4$ on IBM quantum devices. However, the rapid growth of two-qubit gate count and circuit depth makes this Hadamard-test approach impractical for $N > 4$ in our simulations.

To overcome these limitations, we implemented Trotter-error-free time-evolution circuits that directly simulate the quench dynamics and applied randomized measurement techniques. We performed random Pauli measurements (sampling each qubit in the X -, Y - and Z -basis) [43] and extracted the dynamical observables through post-processing using both the Hamming distance method [40, 41] and the classical shadow technique [43, 44]. The results for system sizes up to $N = 12$ obtained from these two post-processing schemes agree closely with each other and show overall good agreement with exact solutions, even without additional error mitigation.

Several directions merit further exploration. Establishing a complete characterization of the system-size dependence of Loschmidt zeros and their corresponding critical times would provide deeper insight into finite-size effects in quench dynamics [60–62]. Finite-rate quenches, in which systems' parameters change gradually over a finite time, also present interesting avenues for extending this work [73–76]. For quantum hardware implementations, shallow-circuit variants of the Hadamard test could enable amplitude estimation for intermediate system sizes [77–82]. Developing scalable, hardware-efficient protocols for measuring Loschmidt echoes and probing dynamical phase transitions remains an important challenge for using noisy intermediate-scale quantum devices in

studies of non-equilibrium phenomena.

ACKNOWLEDGMENTS

We are grateful to Balázs Dóra for valuable discussions. We acknowledge support from the IBM Q Hub at National Taiwan University, the National Science and Technology Council (NSTC), and the National Center for Theoretical Sciences. Y.C.L. was supported by the NSTC under Grants No. NSTC 114-2119-M-007-013 and 113-2119-M-007-013; she is grateful to H.-C. Hsu and H.-C. Chang for previous collaboration. F.I. was supported by the Hungarian Scientific Research Fund under Grant No. K146736 and by the National Research, Development and Innovation Office of Hungary (NKFIH) within the Quantum Information National Laboratory of Hungary; he also acknowledges travel support from the NSTC and National Chengchi University.

Appendix A: Entanglement entropy for $n = 4$ XX- and XXX-chains

In this Appendix, we provide the analytical expressions for the dynamical von Neumann EE for the $n = 4$ XX- and XXX-chains, i.e. with $\Delta = 0$ and $\Delta = 1$.

For the $n = 4$ XX chain, the eigenvalues of the reduced density matrix for a half-chain are given by

$$\begin{aligned}\lambda_{1,2} &= \frac{1}{2} \left[\cos^2 \frac{Jt}{2} + \frac{1}{8} \sin^4 \frac{Jt}{2} \pm \sqrt{\cos^2 \frac{Jt}{2} + \frac{1}{4} \sin^4 \frac{Jt}{2}} \right], \\ \lambda_{3,4} &= \frac{1}{16} \left[1 - \cos^4 \frac{Jt}{2} \pm \sqrt{1 - 2 \cos^4 \frac{Jt}{2} + \cos^8 \frac{Jt}{2} - \sin^8 \frac{Jt}{2}} \right], \\ \lambda_5 &= \frac{1}{16} \sin^4 \frac{Jt}{2}.\end{aligned}\quad (\text{A1})$$

Here, λ_1 and λ_2 are non degenerate, λ_3 and λ_4 are both 4-fold degenerate and λ_5 is 6-fold degenerate. From Eq. (21), we obtain the half-chain von Neumann EE at time t :

$$\mathcal{S}_{1,\text{XX}}^{n=4}(t) = -4 \left[\sin^2 \frac{Jt}{4} \log_2 \sin^2 \frac{Jt}{4} + \cos^2 \frac{Jt}{4} \log_2 \cos^2 \frac{Jt}{4} \right]. \quad (\text{A2})$$

For the XXX chain, the eigenvalues of the reduced density matrix for a half-chain are

$$\begin{aligned}\lambda_1 &= \frac{1}{16} \sin^4 \frac{Jt}{2}, \\ \lambda_2 &= \frac{1}{16} \sin^2 \frac{Jt}{2} \left(1 + 3 \cos^2 \frac{Jt}{2} \right), \\ \lambda_3 &= \frac{1}{16} \left(1 + 3 \cos^2 \frac{Jt}{2} \right)^2,\end{aligned}\quad (\text{A3})$$

where λ_1 is 9-fold degenerate, λ_2 is 6-fold degenerate and λ_3 is non-degenerate. The half-chain von Neumann EE at time t

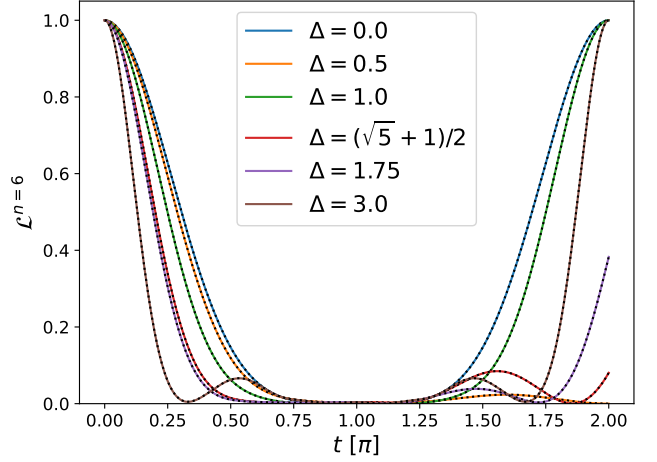


FIG. 18. A comparison of the Loschmidt echo for $n = 6$ and various values of Δ , obtained from Eqs. (B1)-(B3) (solid) and exact diagonalization (dotted), confirming the correctness of the analytical results. The coupling strength is fixed at $J = 1$

is then given by

$$\begin{aligned}\mathcal{S}_{1,\text{XXX}}^{n=4}(t) &= -\frac{3}{2} \sin^2 \frac{Jt}{2} \log_2 \sin^2 \frac{Jt}{2} \\ &\quad - \frac{1}{2} (1 + 3 \cos^2 \frac{Jt}{2}) \log_2 \left(1 + 3 \cos^2 \frac{Jt}{2} \right) + 4.\end{aligned}\quad (\text{A4})$$

Appendix B: Loschmidt echo for $n = 6$

The analytical expression for the Loschmidt echo in the 12-qubit system is given in this Appendix.

By encoding the Bell states in Eq. (7) as $(\psi_0, \psi_1, \psi_2, \psi_3) = (0, 1, 2, 3)$, in Table I we list all products of the Bell dimers for $|\Phi_k\rangle$ that contribute nonzero expansion coefficients $a_k = \langle \Phi_k | \Psi_0 \rangle$, where $|\Psi_0\rangle$ is the initial state in our quench protocol. For each dimer product, the number of equivalent combinations and the corresponding energy $2E_k$ [Eq. (10)] are given in the second and third column of the table, respectively.

From Eq. (37), we obtain the Loschmidt echo in the form:

$$\mathcal{L}^{n=6}(t) = \frac{1}{4^{10}} (cs^2 + s^2). \quad (\text{B1})$$

with

$$\begin{aligned}cs &= \cos [-(6J + 3\Delta J)t/2] + \cos [(6J - 3\Delta J)t/2] \\ &\quad + 15 \cos [-(2J + 3\Delta J)t/2] + 30 \cos [-(4J + \Delta J)t/2] \\ &\quad + 15 \cos [(2J - 3\Delta J)t/2] + 420 \cos [\Delta Jt/2] \\ &\quad + 120 \cos [(2J + \Delta J)t/2] + 120 \cos [(2J - \Delta J)t/2] \\ &\quad + 120 \cos [-(2J + \Delta J)t/2] + 120 \cos [-(2J - \Delta J)t/2] \\ &\quad + 30 \cos [(4J - \Delta J)t/2] + 32 \cos [3\Delta Jt/2],\end{aligned}\quad (\text{B2})$$

TABLE I. Active states with $a_k \neq 0$ for $n = 6$.

dimer product	multiplicity	energy $2E_k$
000000	1	$-6J - 3\Delta J$
111111	1	$6J - 3\Delta J$
222222	1	$3\Delta J$
333333	1	$3\Delta J$
000011	15	$-2J - 3\Delta J$
000022	15	$-4J - \Delta J$
000033	15	$-4J - \Delta J$
001111	15	$2J - 3\Delta J$
001122	90	$-\Delta J$
001133	90	$-\Delta J$
002233	90	$-2J + \Delta J$
112233	90	$2J + \Delta J$
000123	120	$-2J - \Delta J$
011123	120	$2J - \Delta J$
022213	120	ΔJ
033312	120	ΔJ
111122	15	$4J - \Delta J$
111133	15	$4J - \Delta J$
002222	15	$-2J + \Delta J$
003333	15	$-2J + \Delta J$
112222	15	$2J + \Delta J$
113333	15	$2J + \Delta J$
223333	15	$3\Delta J$
332222	15	$3\Delta J$

and

$$\begin{aligned}
si = & \sin [-(6J + 3\Delta J)t/2] + \sin [(6J - 3\Delta J)t/2] \\
& + 15 \sin [-(2J + 3\Delta J)t/2] + 30 \sin [-(4J + \Delta J)t/2] \\
& + 15 \sin [(2J - 3\Delta J)t/2] + 60 \sin [\Delta Jt/2] \\
& + 120 \sin [(2J + \Delta J)t/2] + 120 \sin [(2J - \Delta J)t/2] \\
& + 120 \sin [-(2J + \Delta J)t/2] + 120 \sin [-(2J - \Delta J)t/2] \\
& + 30 \sin [(4J - \Delta J)t/2] + 32 \sin [3\Delta Jt/2] , \quad (\text{B3})
\end{aligned}$$

Figure 18 shows the Loschmidt echo for $n = 6$ with various values of Δ obtained from Eqs. (B1)-(B3) compared with data from exact diagonalization, confirming the correctness of the analytical results.

Appendix C: Loschmidt echo for the XX-chain with $n = 5, 7$ and 9

The analytical expressions of the Loschmidt echo for the XX-chain with $n = 5, 7$ and 9 are given below:

$$\begin{aligned}
\mathcal{L}_{XX}^{n=5}(t) = & \frac{1}{48} [23126 + 31440 \cos(Jt) + 9720 \cos(2Jt) \\
& + 1200 \cos(3Jt) + 50 \cos(4Jt)] , \quad (\text{C1})
\end{aligned}$$

$$\begin{aligned}
\mathcal{L}_{XX}^{n=7}(t) = & \frac{1}{4^{12}} [5015004 + 7604688 \cos(Jt) \\
& + 3281278 \cos(2Jt) + 776776 \cos(3Jt) \\
& + 94276 \cos(4Jt) + 5096 \cos(5Jt) + 98 \cos(6Jt)] , \quad (\text{C2})
\end{aligned}$$

$$\begin{aligned}
\mathcal{L}_{XX}^{n=9}(t) = & \frac{1}{4^{16}} [1134397990 + 1826957088 \cos(Jt) \\
& + 949082256 \cos(2Jt) + 312914784 \cos(3Jt) \\
& + 63548856 \cos(4Jt) + 7564320 \cos(5Jt) \\
& + 487152 \cos(6Jt) + 14688 \cos(7Jt) + 162 \cos(8Jt)] . \quad (\text{C3})
\end{aligned}$$

-
- [1] T. Kinoshita, T. Wenger, and D. S. Weiss, A quantum Newton's cradle, *Nature* **440**, 900 (2006).
- [2] S. Hofferberth, I. Lesanovsky, B. Fischer, T. Schumm, and J. Schmiedmayer, Non-equilibrium coherence dynamics in one-dimensional Bose gases, *Nature* **449**, 324 (2007).
- [3] S. Trotzky *et al.*, Probing the relaxation towards equilibrium in an isolated strongly correlated 1D Bose gas, *Nat. Phys.* **8**, 325 (2012).
- [4] F. Meinert *et al.*, Many-body quantum quench in an atomic one-dimensional Ising chain, *Phys. Rev. Lett.* **111**, 053003 (2013).
- [5] T. Langen *et al.*, Experimental observation of a generalized Gibbs ensemble, *Science* **348**, 207 (2015).
- [6] B. Fauseweh, Quantum many-body simulations on digital quantum computers: State-of-the-art and future challenges, *Nat. Commun.* **15**, 2123 (2024).
- [7] N. Mueller, J. A. Carolan, A. Connelly, Z. Davoudi, E. F. Dumitrescu, and K. Yeter-Aydeniz, Quantum computation of dynamical quantum phase transitions and entanglement tomography in a lattice gauge theory, *PRX Quantum* **4**, 030323 (2023).
- [8] A. Smith, M. S. Kim, F. Pollmann, and J. Knolle, Simulating quantum many-body dynamics on a current digital quantum computer, *npj Quantum Information* **5**, 106 (2019).
- [9] S.-H. Lin, R. Dilip, A. G. Green, A. Smith, and F. Pollmann, Real- and imaginary-time evolution with compressed quantum circuits, *PRX Quantum* **2**, 010342 (2021).
- [10] J. Vovrosh and J. Knolle, Confinement and entanglement dynamics on a digital quantum computer, *Scientific Reports* **11**, 11577 (2021).
- [11] J. Vovrosh, K. E. Khosla, S. Greenaway, C. Self, M. S. Kim, and J. Knolle, Simple mitigation of global depolarizing errors in quantum simulations, *Phys. Rev. E* **104**, 035309 (2021).
- [12] J. M. Koh, T. Tai, and C. H. Lee, Simulation of Interaction-Induced Chiral Topological Dynamics on a Digital Quantum Computer, *Phys. Rev. Lett.* **129**, 140502 (2022).
- [13] H.-C. Chang, H.-C. Hsu, and Y.-C. Lin, Probing entanglement dynamics and topological transitions on noisy intermediate-

- scale quantum computers, *Phys. Rev. Research* **7**, 013043 (2025).
- [14] J. Vovrosh, J. de Hond, S. Juliá-Farré, J. Knolle, A. Dauphin, Meson spectroscopy of exotic symmetries of Ising criticality in Rydberg atom arrays, arXiv:2506.21299 (2025).
- [15] H.-T. Hung, I. N. M. Le, J. Knolle, Y.-J. Kao, Improved Ising Meson Spectroscopy Simulation on a Noisy Digital Quantum Device, arXiv:2512.02516 (2025).
- [16] M. K. Giri and P. Chen, Digital Quantum Simulation of Flat-Band and All-Bands-Flat Dynamics for Tunable Quantum Transport, arXiv:2508.08734 (2025).
- [17] A. Mitra, Quantum Quench Dynamics, *Annual Review of Condensed Matter Physics* **9**, 245 (2018).
- [18] J. M. Deutsch, Quantum statistical mechanics in a closed system, *Phys. Rev. A* **43**, 2046 (1991).
- [19] M. Rigol, V. Dunjko, and M. Olshanii, Thermalization and its mechanism for generic isolated quantum systems, *Nature* **452**, 854 (2008).
- [20] A. Polkovnikov, K. Sengupta, A. Silva, and M. Vengalattore, Colloquium: Nonequilibrium dynamics of closed interacting quantum systems, *Rev. Mod. Phys.* **83**, 863 (2011).
- [21] L. D'Alessio, Y. Kafri, A. Polkovnikov, and M. Rigol, From quantum chaos and eigenstate thermalization to statistical mechanics and thermodynamics, *Adv. Phys.* **65**, 239 (2016).
- [22] M. A. Cazalilla, Effect of suddenly turning on interactions in the Luttinger model, *Phys Rev Lett* **97**, 156403 (2006).
- [23] M. Rigol, A. Muramatsu, and M. Olshanii, Hard-core bosons on optical lattices: Dynamics and relaxation in the superfluid and insulating regimes, *Phys. Rev. A* **74**, 053616 (2006).
- [24] M. Rigol, V. Dunjko, V. Yurovsky, and M. Olshanii, Relaxation in a completely integrable many-body quantum system: An ab initio study of the dynamics of the highly excited states of 1D lattice hard-core bosons, *Phys. Rev. Lett.* **98**, 050405 (2007).
- [25] P. Calabrese, F. H. L. Essler, M. Fagotti, Quantum quench in the transverse-field Ising chain, *Phys Rev Lett* **106**, 227203 (2011).
- [26] J.-S. Caux and F. H. L. Essler, Time evolution of local observables after quenching to an integrable model, *Phys. Rev. Lett.* **110**, 257203 (2013).
- [27] B. Wouters, J. De Nardis, M. Brockmann, D. Fioretto, M. Rigol, and J.-S. Caux, Quenching the Anisotropic Heisenberg Chain: Exact Solution and Generalized Gibbs Ensemble Predictions, *Phys. Rev. Lett.* **113**, 117202 (2014).
- [28] E. Ilievski, J. De Nardis, B. Wouters, J.-S. Caux, F. H. L. Essler, and T. Prosen, Complete Generalized Gibbs Ensembles in an Interacting Theory, *Phys. Rev. Lett.* **115**, 157201 (2015).
- [29] F. H. L. Essler, G. Mussardo, and M. Panfil, Generalized Gibbs ensembles for quantum field theories, *Phys. Rev. A* **91**, 051602(R) (2015).
- [30] M. Kormos, M. Collura, G. Takács, and P. Calabrese, Real time confinement following a quantum quench to a non-integrable model, *Nat. Phys.* **13**, 246 (2017).
- [31] O. A. Castro-Alvaredo, M. Lencsés, I. M. Szécsényi, and J. Viti, Entanglement Oscillations near a Quantum Critical Point, *Phys. Rev. Lett.* **124**, 230601 (2020).
- [32] T. Chanda, J. Zakrzewski, M. Lewenstein, and L. Tagliacozzo, Confinement and Lack of Thermalization After Quenches in the Bosonic Schwinger Model, *Phys. Rev. Lett.* **124**, 180602 (2020).
- [33] R. Menu and T. Roscilde, Quench dynamics of quantum spin models with flat bands of excitations, *Phys. Rev. B* **98**, 205145 (2018).
- [34] J. G. C. Martinez *et al.*, Flat-band localization and interaction-induced delocalization of photons, *Sci. Adv.* **9**, ead7195 (2023).
- [35] S. Ziraldo, and G. E. Santoro, Relaxation and thermalization after a quantum quench: Why localization is important, *Phys. Rev. B* **87**, 064201 (2013).
- [36] H. Wilming, T. J. Osborne, K. S. C. Decker, et al. Reviving product states in the disordered Heisenberg chain, *Nat Commun* **14**, 5847 (2023).
- [37] C. J. Turner, A. A. Michailidis, D. A. Abanin, M. Serbyn, Z. Papić, Quantum many-body scars, *Nat. Phys.* **14**, 745 (2018).
- [38] N. O'Dea and A. Sriram, Entanglement Oscillations from Many-Body Quantum Scars, *Phys. Rev. Lett.* **134**, 210402 (2025).
- [39] R. Cleve, A. Ekert, C. Macchiavello, and M. Mosca, Quantum algorithms revisited, *Proc. R. Soc. A* **454**, 339 (1998).
- [40] B. Vermersch, A. Elben, M. Dalmonte, J. I. Cirac, and P. Zoller, Unitary n-designs via random quenches in atomic Hubbard and spin models: Application to the measurement of Rényi entropies, *Phys. Rev. A* **97**, 023604 (2018).
- [41] T. Brydges, A. Elben, P. Jurcevic, B. Vermersch, C. Maier, B. P. Lanyon, P. Zoller, R. Blatt, and C. F. Roos, Probing Rényi entanglement entropy via randomized measurements, *Science* **364**, 260 (2019).
- [42] A. Elben, B. Vermersch, C. F. Roos, and P. Zoller, Statistical correlations between locally randomized measurements: A toolbox for probing entanglement in many-body quantum states, *Phys. Rev. A* **99**, 052323 (2019).
- [43] H.-Y. Huang, R. Kueng, and J. Preskill, Predicting many properties of a quantum system from very few measurements. *Nat. Phys.* **16**, 1050 (2020).
- [44] A. Elben, S. T. Flammia, H.-Y. Huang, R. Kueng, B. Vermersch, and P. Zoller, The randomized measurement toolbox, *Nature Reviews Physics* **5**, 9 (2023).
- [45] E. Lieb, T. Schultz, and D. Mattis, Two Soluble Models of an Antiferromagnetic Chain, *Annals of Physics* **16**, 407 (1961).
- [46] W. P. Su, J. R. Schrieffer, and A. J. Heeger, Solitons in Polyacetylene, *Phys. Rev. Lett.* **42**, 1698 (1979).
- [47] H. Bethe, Zur Theorie der Metalle. I. Eigenwerte und Eigenfunktionen der linearen Atomkette, *Z. Phys.* **71**, 205 (1931).
- [48] E. Pytte, Peierls instability in Heisenberg chains, *Phys. Rev. B* **10**, 4637 (1974).
- [49] M. C. Cross and D. S. Fisher, A new theory of the spin-Peierls transition with special relevance to the experiments on TTFCuBDT, *Phys. Rev. B* **19**, 402 (1979).
- [50] B. Sutherland, Systems with resonating-valence-bond ground states: Correlations and excitations, *Phys. Rev. B* **37** 3786 (1988).
- [51] K. S. D. Beach, A. W. Sandvik, Some formal results for the valence bond basis, *Nuclear Physics B* **750** 142 (2006).
- [52] Z. Gong and M. Ueda, Topological entanglement-spectrum crossing in quench dynamics, *Phys. Rev. Lett.* **121**, 250601 (2018).
- [53] M. Heyl, A. Polkovnikov, and S. Kehrein, Dynamical Quantum Phase Transitions in the Transverse-Field Ising Model, *Phys. Rev. Lett.* **110**, 135704 (2013).
- [54] C. Karrasch and D. Schuricht, Dynamical Phase Transitions after Quenches in Nonintegrable Models, *Phys. Rev. B* **87**, 195104 (2013).
- [55] M. Heyl, Dynamical Quantum Phase Transitions in Systems with Broken-Symmetry Phases, *Phys. Rev. Lett.* **113**, 205701 (2014).
- [56] F. Andraschko and J. Sirker, Dynamical Quantum Phase Transitions and the Loschmidt Echo: A Transfer Matrix Approach, *Phys. Rev. B* **89**, 125120 (2014).
- [57] S. Vajna and B. Dóra, Disentangling Dynamical Phase Transitions from Equilibrium Phase Transitions, *Phys. Rev. B* **89**, 161105 (2014).

- [58] A. A. Zvyagin, Dynamical Quantum Phase Transitions (Review Article), *J. Low Temp. Phys.* **42**, 971 (2016).
- [59] M. Heyl, Dynamical quantum phase transitions: a review, *Rep. Prog. Phys.* **81** 054001 (2018).
- [60] B. Zhou, Y. Zeng, and S. Chen, Exact zeros of the Loschmidt echo and quantum speed limit time for the dynamical quantum phase transition in finite-size systems, *Phys. Rev. B* **104**, 094311 (2021).
- [61] Y. Zeng, B. Zhou, and S. Chen, Dynamical singularity of the rate function for quench dynamics in finite-size quantum systems, *Phys. Rev. B* **107**, 134302 (2023).
- [62] D. P.-García, L. Santilli, and M. Tierz, Dynamical quantum phase transitions from random matrix theory, *Quantum* **8**, 1271 (2024).
- [63] V. Eisler and I. Peschel, Entanglement in a periodic quench, *Ann. Phys. (Berlin)* **17**, 410 (2008).
- [64] S. Vajna and B. Dora, Topological classification of dynamical phase transitions, *Phys. Rev. B* **91** 155127 (2015).
- [65] F. Iglói, R. Juhász, and H. Rieger, Random antiferromagnetic quantum spin chains: Exact results from scaling of rare regions, *Phys. Rev. B* **61** 11552 (2000).
- [66] F. Iglói and R. Juhász, Exact relationship between the entanglement entropies of XY and quantum Ising chains, *EPL* **81**, 57003 (2008).
- [67] R. Verresen, R. Moessner, and F. Pollmann, One-dimensional symmetry protected topological phases and their transitions, *Phys. Rev. B* **96**, 165124 (2017).
- [68] M. Heyl, Scaling and Universality at Dynamical Quantum Phase Transitions, *Phys. Rev. Lett.* **115** 140602 (2015).
- [69] A. Javadi-Abhari, et al., Quantum Computing with Qiskit, *arXiv:2405.08810* (2024).
- [70] Z. Cai, et al. Quantum error mitigation, *Rev. Mod. Phys.* **95** 045005 (2023).
- [71] H. F. Trotter, On the product of semi-groups of operators, *Proc. Am. Math. Soc.* **10**, 545 (1959).
- [72] The software package is available at: <https://github.com/qurrium/qurrium>.
- [73] R. Schützhold, M. Uhlmann, Y. Xu, and U. R. Fischer, Sweeping from the Superfluid to the Mott Phase in the Bose-Hubbard Model, *Phys. Rev. Lett.* **97**, 200601 (2006).
- [74] M. Uhlmann, R. Schützhold, and U. R. Fischer, Vortex Quantum Creation and Winding Number Scaling in a Quenched Spinor Bose Gas, *Phys. Rev. Lett.* **99**, 120407 (2007).
- [75] F. Pellegrini, S. Montangero, G. E. Santoro, and R. Fazio, Adiabatic quenches through an extended quantum critical region, *Phys. Rev. B* **77**, 140404(R) (2008).
- [76] S. Sharma, U. Divakaran, A. Polkovnikov, and A. Dutta, Slow quenches in a quantum Ising chain: Dynamical phase transitions and topology, *Phys. Rev. B* **93**, 144306 (2016).
- [77] H. Ni, H. Li, and L. Ying, On low-depth algorithms for quantum phase estimation, *Quantum* **7**, 1165 (2023).
- [78] Y. Yang, A. Christianen, M. C. Bañuls, D. S. Wild, and J. I. Cirac, Phase-Sensitive Quantum Measurement without Controlled Operations, *Phys. Rev. Lett.* **132**, 220601 (2024).
- [79] B. F. Schiffer, D. S. Wild, N. Maskara, M. D. Lukin, J. I. Cirac, Hardware-efficient quantum phase estimation via local control, *arXiv:2506.18765* (2025).
- [80] L. C. Tazi, D. M. Ramo, A. J. W. Thom, Shallow Quantum Scalar Products with Phase Information, *arXiv:2411.19072* (2024).
- [81] C. Lenihan, et al, Excitation Amplitude Sampling for Low Variance Electronic Structure on Quantum Computers, *arXiv:2506.15438* (2025).
- [82] E. Mastorakis, et al, Resource-efficient Hadamard test tailored variational framework for nonlinear dynamics on quantum computers, *Quantum Sci. Technol.* **11** 015061 (2026).